Journal of Atmospheric and Solar-Terrestrial Physics ∎ (∎∎∎∎) ∎∎∎–∎∎∎

Contents lists available at ScienceDirect

Journal of Atmospheric and Solar-Terrestrial Physics

journal homepage: www.elsevier.com/locate/jastp

Detection of meteoric smoke particles in the mesosphere by a rocket-borne mass spectrometer

Scott Robertson [a], Shannon Dickson [a,*], Mihaly Horányi [a], Zoltan Sternovsky [a], Martin Friedrich [b], Diego Janches [c], Linda Megner [d], Bifford Williams [e]

[a] University of Colorado, Boulder, CO 80304, USA
[b] Graz University of Technology, 8010 Graz, Austria
[c] Goddard Space Flight Center, Greenbelt, MD 20771, USA
[d] Department of Meteorology, Stockholm University, 106 91 Stockholm, Sweden
[e] GATS-Inc., Boulder, CO 80301, USA

ARTICLE INFO

Article history:
Received 11 March 2013
Received in revised form
10 July 2013
Accepted 15 July 2013

Keywords:
Mesosphere
Charged MSPs
In situ data
Mass spectrometer

ABSTRACT

In October 2011, two CHAMPS (Charge And Mass of meteoric smoke ParticleS) sounding rockets were launched into the polar mesosphere, each carrying an electrostatic multichannel mass analyzer for charged meteoric smoke particles (MSPs) that operated from 60 to 100 km and returned data on the number density of the charged MSPs in several ranges of mass. The payloads also carried Faraday rotation antennas and an array of plasma probes for determining electron and ion densities and the payload charging potential, thus providing a comprehensive picture of the distribution of charges over a wide range of altitudes that can be compared with models for the vertical distribution of MSPs and for the distribution of charge. The launches were from the Andøya Rocket Range, Norway, following the end of the noctilucent cloud season to avoid detection of ice. A night launch (11 October 21:50 UT) and a day launch (13 October 13:50 UT) helped to elucidate the role of solar ultraviolet in determining the charge state of the particles. The night data show a distinct change in the charge state of MSPs at the D-region ledge (~78 km) below which the density of free electrons is greatly reduced. Above the ledge, negative MSPs are detected at up to 92 km, have number densities reaching ~200 cm^{-3}, and positive MSPs are absent. Below the ledge, positive and negative MSPs are about equally abundant, each with densities of ~2000 cm^{-3} at 70 km and with slightly lower densities at 60 km. The MSPs are seen predominantly in mass bins spanning 500–2000 amu and 2000–8000 amu, with more massive particles (radii above ~1.2 nm assuming a smoke particle density of 2 g/cm^3) having number densities below the detection threshold (10 cm^{-3}) and less massive particles being indistinguishable from ions. The daytime launch data show positive MSPs present only below the ledge and their number density is reduced to below 300 cm^{-3}. The daytime data show negative MSPs both above and below the D-region ledge and their number density is also reduced, perhaps as a consequence of photodetachment. Modeling of the charge state of the MSPs shows that the total number density of MSPs, charged and uncharged, is approximately 20,000 cm^{-3} below the ledge and the model reproduces the absence of positive MSPs above the ledge.

1. Introduction

In the last decade, advances in instrumentation have made it possible to detect the meteoric smoke particles (MSPs) from the ablation of meteors in the upper atmosphere. The new methods include rocket-borne instruments, ground-based radar, and remote sensing by satellite. We report results from a 10-channel rocket-borne mass spectrometer that simultaneously records the number density of charged nanometer-sized particles in five mass ranges for both signs of charge. The design has sampled air flowing through the instrument thus allowing the detection of the smallest particles which might otherwise be carried around the instrument by aerodynamics. These measurements of the number density of MSPs are the first with mass resolution and they extend over a greater range of altitude (60–90 km) than previous in situ measurements. Number densities of positively and negatively charged particles are measured separately and the uncharged fraction is deduced from a charging model. Two nearly identical payloads, also carrying a variety of other instruments to aid in data interpretation, were launched from Andøya Rocket Range, Norway, one in daytime and one at night in order to help elucidate the role

* Correspondence to: Center for Integrated Plasma Studies, University of Colorado, UCB 390, Boulder, CO 80309-0390, USA. Tel.: +1 303 735 4305.
E-mail address: Scott.Robertson@colorado.edu (S. Robertson).

1364-6826/$ - see front matter © 2013 Elsevier Ltd. All rights reserved.
http://dx.doi.org/10.1016/j.jastp.2013.07.007

of photoelectron emission and photodetachment in determining the charge state of the particles.

Meteoric smoke particles are the likely condensation nuclei for noctilucent clouds (NLC) (Witt, 1969). Rosinski and Snow (1961) modeled the formation of meteoric smoke particles in the meteor trail. Plane (2003) has argued that smoke particles do not form in the meteor trails but form after the trail has dispersed by polymerization of reaction products with large dipole moments. Recent work on the ablation process includes detailed modeling (Vondrak et al., 2008) and observations (Janches et al., 2009) of differential ablation that show Na and K evaporating about 12 km higher (100–110 km) than the more refractory Si, Fe, and Mg. There have also been flow tube studies of the molecular species likely to be formed by chemical reactions of the metal atoms from ablation (Saunders and Plane, 2006). Regardless of composition, models (Hunten et al., 1980; Megner et al., 2006; Bardeen et al., 2008) have shown that there are several tens of thousands of nanometer-sized particles per cubic centimeter throughout the mesosphere and upper stratosphere. These results are strongly dependent upon assumptions that include an initial mean particle size of 0.2 nm and a vapor number density adjusted to be consistent with a mean flux of 44 t/day (Hughes, 1978; Megner et al., 2008a), which has a large uncertainty (Plane, 2012). These models suggest that the highest number densities occur at 80–90 km above which there is a sharp depletion in abundance. Since the ablation profile depends on uncertain properties such as the meteor velocity distribution, the altitude of this upper limit could be anywhere between 85 and 105 km (Kalashnikova et al., 2000; Megner et al., 2006). Below 80 km, the models show a decreasing number density due to coagulation and sedimentation as well as latitudinal and seasonal variations from atmospheric circulation.

Observations of meteoric material have been made by airborne instruments in the Arctic stratosphere below 14 km in winter, when mesospheric air is transported downward (Curtius et al., 2005). The transported particles have implications for polar stratospheric clouds, sulfate aerosols and ozone chemistry. Observations of Ir and Pt in Greenland ice cores are consistent with an origin in meteoric smoke particles (Gabrielli et al., 2004). The presence of meteoric smoke particles above 60 km altitude has been detected by measurements of optical extinction by the Solar Occultation for Ice Experiment (SOFIE) instrument on the AIM (Aeronomy of Ice in the Mesosphere) spacecraft (Hervig et al., 2009). These extinction data also placed constraints on the composition of the smoke particles (Hervig et al., 2012). Evidence for MSPs has also been seen in data from the incoherent scatter radar at Arecibo, Puerto Rico. The data had sufficient signal to noise ratio in the range 80–95 km to deduce particle characteristic radii and number densities. Strelnikova et al. (2007) found number densities rising from $\sim$10 cm^{-3} at 85 km to $\sim$1000 cm^{-3} at 90 km whereas Fentzke et al. (2009, 2012) found densities rising from $\sim$300 cm^{-3} at 80 km to $\sim$20,000 cm^{-3} at 94 km with little seasonal variation, as would be expected at midlatitudes. Both studies indicated a characteristic radius of approximately 1 nm.

While there is substantial evidence of MSP occurrence at NLC altitudes, atmospheric circulation models have recently shown a strong seasonal variation in the density of MSPs sufficiently large to be condensation nuclei for NLCs. MSPs less than 1 nm in radius are thought to be ineffective as nuclei because of the Kelvin barrier. Megner et al. (2006, 2008a, 2008b) coupled the Community Aerosol Radiation Model for Atmospheres (CARMA) for smoke production and sedimentation with the CHEM2D model for circulation and showed that at the summer pole the number density of particles greater than 1 nm in radius is reduced to below 10 cm^{-3} as a consequence of meridional circulation. This seasonal reduction was also seen by Bardeen et al. (2008) who coupled the CARMA model with the three-dimensional Whole Atmosphere Community Climate Model (WACCM) for circulation. The predicted summer reduction in the density of MSPs above 60 km altitude has been seen in measurements of optical extinction (Hervig et al., 2009). The models suggest that the sufficiently large MSPs are too few to serve as condensation nuclei for NLCs or for the subvisual icy particles causing the radar returns called polar mesospheric summer echoes (PMSE) (Rapp and Lübken, 2004). Gumbel and Megner (2009) and Megner and Gumbel (2009) have pointed out that the Kelvin barrier is removed if the particles are charged; thus allowing the more numerous smaller particles to serve as condensation nuclei if charged. Plane (2011) has argued that metal silicates have sufficient dipole moments to remove the barrier in the absence of charge.

The altitudes at which MSPs and ice particles occur include the D region of the ionosphere where there are sufficient numbers of free electrons and ions for a significant fraction of these particles to be charged (Reid, 1990; Havnes et al., 1990; Jensen and Thomas, 1991). Initial modeling, which assumed a much greater number of free electrons than of particles, showed that nearly all of the particles would be negatively charged due to the greater rate coefficient for the attachment of electrons. Polar mesospheric winter echoes (PMWE), much weaker than PMSE, have been seen in disturbed conditions with high electron densities in winter at 55–80 km altitude. These have been attributed to the attachment of electrons to MSPs with particle radius near 3 nm (Kavanagh et al., 2006; La Hoz and Havnes, 2008; Havnes and Kassa, 2009; Havnes et al., 2011). Modeling for a wider range of conditions has shown that for low ionization rates and large numbers of particles both the electron and the ion from an ionization event would each attach to a MSP making the numbers of positive and negative particles more nearly equal (Reid, 1997; Rapp and Lübken, 2001).

The first in situ observations of charged meteoric smoke in the mesosphere were made using the rocket-borne Faraday cups that had been developed for the detection of charged NLC particles (Havnes et al., 1996). Modeling of the air flow in and around Faraday cups has shown that nanometer-sized particles (but not the larger NLC particles) are carried around the cup entrance by the air flow which results in reduced sensitivity to these particles (Hedin et al., 2007) that is dependent upon altitude and velocity. Measurements of MSPs were initially made at tropical latitudes (Puerto Rico) where temperatures in the mesosphere rule out the possibility of observed particles being ice (Gelinas et al., 1998) and above Alaska outside the season in which icy particles could occur (Lynch et al., 2005; Gelinas et al., 2005). Amyx et al. (2008), using a dust impact detector, found net positively charged particles with densities of $\sim$1000 cm^{-3} at 80–85 km altitude above Scandinavia after the NLC season. Rapp et al. (2007) have reviewed in situ measurements including data from mass spectrometers and Gerdien condensers that had much earlier indicated charged species too massive to be identified as molecular ions.

Rapp et al. (2003) developed a rocket-borne instrument for detection of MSPs utilizing an ultraviolet flashlamp coupled with a Faraday cup. The lamp caused photodetachment of electrons from the negatively charged smoke particles and possibly photoemission from neutral particles. A fast burst of electrons from photodetachment was detected by the Faraday cup as well as a continuous (DC) signal from the charged smoke. The DC signal was attributed to smoke particles greater than about 2 nm in radius because the smaller particles would be carried around the instrument by aerodynamic effects. The instrument was flown on several rockets as part of the ECOMA (Existence and Charge state of Meteoric smoke particles in the middle Atmosphere) campaign from the Andøya Rocket Range, with some flights within the NLC season and some outside the season (Rapp et al., 2009, 2010, 2012; Rapp and Strelnikova, 2009; Strelnikova et al., 2009). Data from three flights in 2010 (before, during, and after the Geminid meteor shower) showed electron release from negative MSPs from 87 to

Please cite this article as: Robertson, S., et al., Detection of meteoric smoke particles in the mesosphere by a rocket-borne mass spectrometer. Journal of Atmospheric and Solar-Terrestrial Physics (2013), http://dx.doi.org/10.1016/j.jastp.2013.07.007

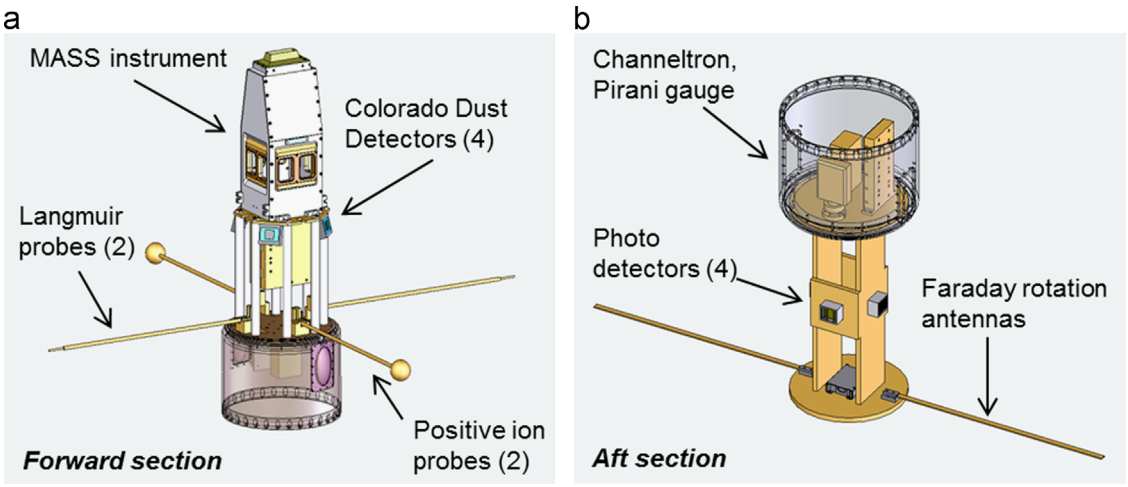

Fig. 1. The CHAMPS (a) forward and (b) aft payload sections.

95 km. The work functions for the particles were determined to be in the range 4–4.6 eV through the use of flashlamps with spectra having different cutoffs in the ultraviolet. The ECOMA rockets also carried Faraday cups for recording charged MSPs, but the number densities obtained were a lower bound because of aerodynamics reducing the sensitivity.

Our new measurements of MSPs by the rocket-borne mass spectrometer are described in the sections below. The payload instruments are described in Section 2 and the data are presented in Section 3. Section 4 presents results from two models: a charging model which aids in data interpretation and an atmospheric model combining coagulation, sedimentation, and circulation which finds the expected altitudes and number densities of MSPs. Section 5 is a discussion of the data, its relationship to previous measurements, and implications for future measurements and modeling.

2. The CHAMPS instruments

The two nearly identical CHAMPS (Charge And Mass of meteoric smoke ParticleS) payloads, Fig. 1, had a forward experiment section uncovered by a deployable nosecone and an aft experiment section uncovered by an aft skirt. The payloads were 4.4 m in length after the deployments and 35.6 cm in diameter, excluding the extended booms. The payload carried an attitude control system that pointed the payload axis to within 1.3° of the ram direction on both the upleg and downleg. The two-stage rocket was a Terrier MK12-Improved Orion configuration with a spin rate of 2 Hz.

The instruments in the forward payload section were the aerosol particle mass spectrometer (MASS), four Colorado dust detectors (CDD), a pair of positive ion probes (PIP), a Langmuir probe with a fixed bias voltage for collecting ions, and a Langmuir probe with a swept bias voltage to determine the payload potential. The aft section carried a pair of antennas for Faraday rotation measurement of electron density and photoemission detectors to help determine the role of photoemission in creating spurious signals from the charge collectors. A ground-based lidar was used for atmospheric sodium density and temperature measurements.

The aft payload section also carried instruments with secondary objectives not directly related to meteoric smoke. These included a channel electron multiplier and an adjacent Pirani gauge to determine on the downleg the altitude below which the pressure becomes too large to permit electron multiplier operation. This was done to determine if it is possible for an electron multiplier to be used as a more sensitive detector of charged particles without employing a vacuum pump. The results of this test have been reported separately (Dickson et al., 2013).

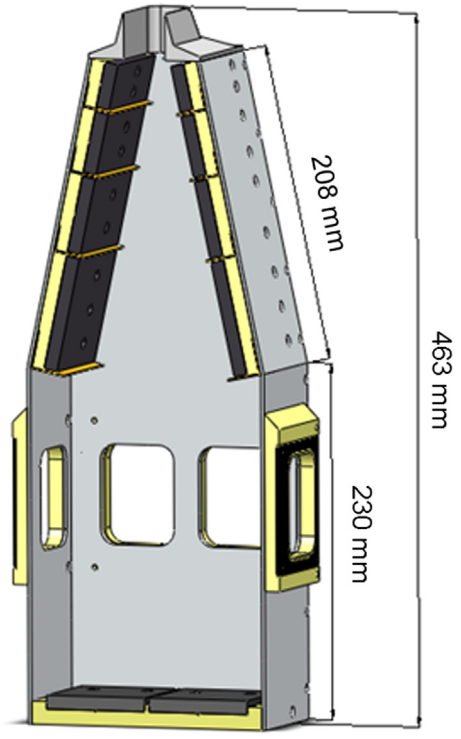

Fig. 2. Engineering drawing (cross section) of the MASS spectrometer showing the five collector electrodes on each side and the air exit windows. The bias voltages on the top four electrodes are approximately ±4 V, ±10 V, ±30 V and ±54 V.

2.1. The MASS instrument

2.1.1. Principles of operation

The MASS instrument (Mesospheric Aerosol Sampling Spectrometer) used for CHAMPS is a 10-channel electrostatic mass spectrometer that simultaneously records the charge collected in five ranges of mass for both positively and negatively charged aerosol particles, Fig. 2. Two 8-channel MASS instruments were flown in 2007 into NLC conditions and into PMSE conditions and successfully returned data on the mass, number density, and charge state of the icy particles responsible for these phenomena (Robertson et al., 2009). The instrument uses electrostatic deflection to determine the mass of

Please cite this article as: Robertson, S., et al., Detection of meteoric smoke particles in the mesosphere by a rocket-borne mass spectrometer. Journal of Atmospheric and Solar-Terrestrial Physics (2013), http://dx.doi.org/10.1016/j.jastp.2013.07.007

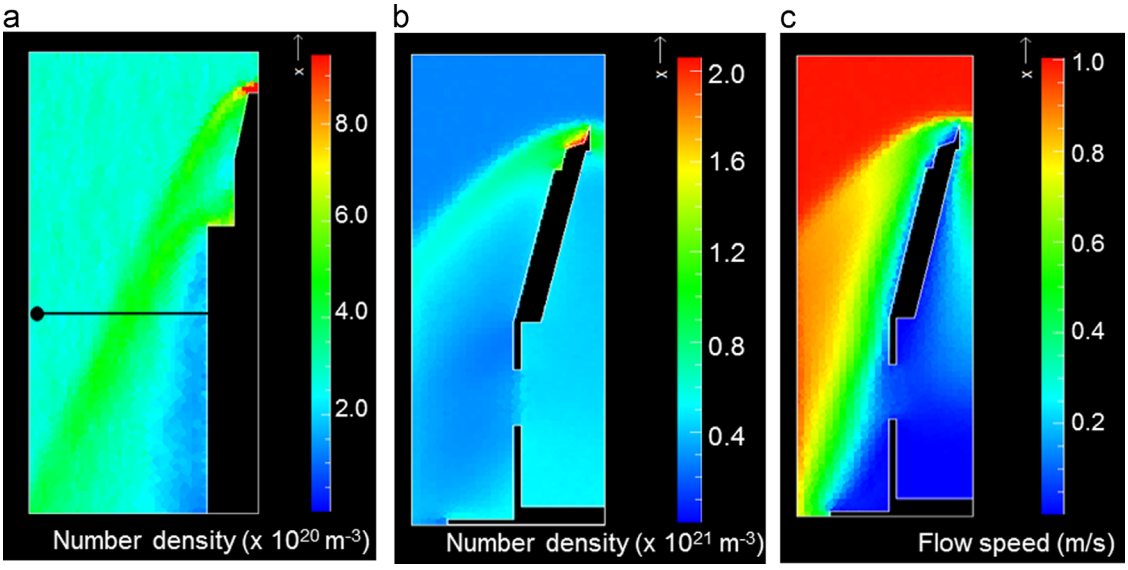

Fig. 3. (a) DSMC simulation of the air number density around the payload showing the shock wave position relative to the tips of the probes. (b) Detail of the DSMC simulation showing the number density of air within the MASS instrument. (c) Detail of the DSMC simulation showing the flow speed within the MASS instrument.

incident particles. The particles entering a slit (28 mm × 90 mm) at the top of the instrument are electrostatically deflected onto collection plates (electrodes) located at increasing distances from the slit and with increasing bias voltages. The charged particles deposit their charge on the electrodes and the current is measured by sensitive electrometers. The collectors on one side of the instrument have positive bias voltages to attract negative particles and the collectors on the opposite side have negative voltages to attract positive particles. An unbiased pair of collectors on the bottom of the instrument detects heavier undeflected particles; however, such heavy particles are not expected in the absence of NLC. Deflection of a singly charged particle is determined by its kinetic energy which depends upon its mass and the rocket velocity (with only a small contribution from its thermal velocity). Particles with sizes of the order of nanometers are unlikely to be multiply charged (Rapp and Lübken, 2001); hence the mass is simply related to the deflection. Details of the construction are given in Knappmiller et al. (2008).

The MASS instrument also has windows on all four sides near the bottom to exhaust the inflowing air. The flow streamlines from direct simulation Monte-Carlo (DSMC) simulations (Bird, 1988, 1994) show that the air directly above the slit entrance flows into the slit, through the instrument, and out through the windows. This is in contrast to DSMC results for Faraday cups with closed bottoms which fill with stagnant air causing the upstream air and entrained low-mass particles to flow around the entrance (Hedin et al., 2007).

2.1.2. Calibration

The range of masses falling on each electrode is determined by three sets of numerical simulations. In the first set, the density, temperature and velocity of the air flowing around and through the instrument are found by the DSMC method for altitudes spanning 65 km to 90 km. The upstream atmospheric density and temperature at each altitude are taken from the MSIS-E-90 Atmosphere Model using daytime autumn conditions for 69°N latitude. (Daytime and nighttime number densities and temperatures are approximately equal at the modeled altitudes.) The output of the DSMC code is the air flow velocity vector, temperature, and number density on a spatial grid with a resolution of a few millimeters. Fig. 3a shows the flow around the forward payload section at 80 km. Fig. 3b shows the air density within the MASS instrument and Fig. 3c shows the flow speed in and around the instrument, also at 80 km. For the conditions simulated, the number density is 2.8×10^{14} cm^{-3} upstream of the slit entrance and increases to 5.1×10^{14} cm^{-3} at the bottom of the instrument. The axial air flow speed drops from 994 m/s to 500 m/s abruptly at the shock and then falls gradually to 100 m/s at the exit windows.

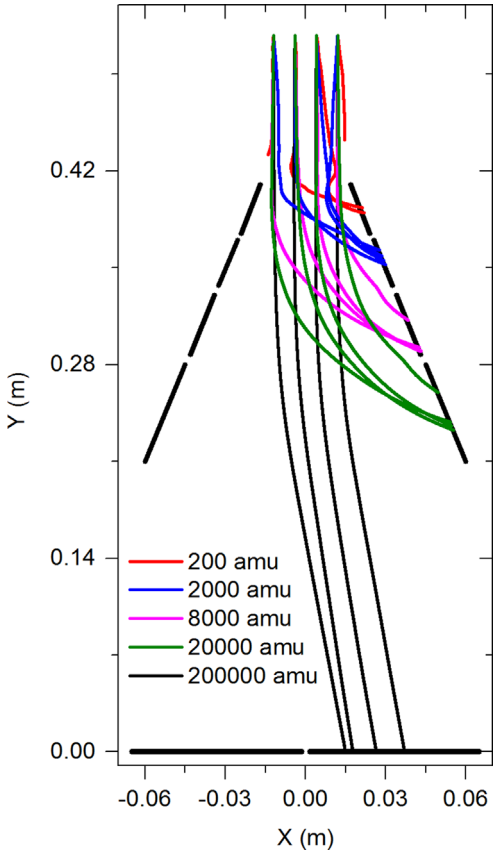

Fig. 4. Trajectories within the MASS instrument of singly charged particles of different masses. These computer generated trajectories are used to determine the range of mass collected by each electrode.

Please cite this article as: Robertson, S., et al., Detection of meteoric smoke particles in the mesosphere by a rocket-borne mass spectrometer. Journal of Atmospheric and Solar-Terrestrial Physics (2013), http://dx.doi.org/10.1016/j.jastp.2013.07.007

In the second set of simulations, Poisson's equation is solved within the instrument to find the electric field and hence the electric force acting on a particle at any location. The first pair of electrodes is biased approximately to ± 4 V, the second pair to ± 10 V, the third pair to ± 30 V, and the fourth pair to ± 54 V. The third set of numerical simulations is done to find the trajectories of charged smoke particles of a specified mass. The particles are acted upon by the deflecting electric field and by Monte-Carlo collisions with air molecules. The air molecules used for the collisions are chosen from a distribution function that has the flow velocity, density, and temperature found by the DSMC code (Knappmiller et al., 2008). The smoke particles are placed on a grid above the instrument with an initial velocity downward having the same magnitude as the rocket velocity. Equations of motion are integrated numerically to find the trajectories of the particles within the instrument. A typical set of trajectories is shown in Fig. 4. The effect of collisions is most visible in the trajectories of the smallest smoke particles (less than about 1000 amu in mass) because larger particles have their trajectories altered only slightly by collisions with the much lighter air molecules.

The trajectory simulations are used to find the collection efficiency for each electrode which is used to convert the measured current into a charge number density. The collection efficiency is defined as the number of particles of a given mass hitting an electrode divided by the number launched in the volume upstream of the slit. Particles outside of the region directly upstream of the slit are included to account for scattering events causing particles to enter the slit that would otherwise have been missed. The number density of charged MSP particles is found from flight data using $n=I/(qvAf)$, where n is the number density, I is the collected current, q is the elementary charge, v is the rocket speed, A is the slit area, and f is the collection efficiency.

The collection efficiency calculations were done for altitudes of 65, 70, 75, 80, and 90 km. There are three parameters that cause the collection efficiency curves to vary with altitude: rocket velocity, air density, and payload potential. (1) At higher altitudes, the rocket slows and particles enter the instrument with smaller velocities, their deflection is increased, and this moves their point of collection nearer to the entrance slit. (2) The air density changing with altitude causes the collision frequency to vary. The effect of collisions is to reduce the resolution of the instrument by causing particles of the same mass that begin on identical trajectories to be collected by different electrodes. This reduced resolution also decreases the peak collection efficiency, with the effect being the greatest for the lowest masses. (3) The payload potential accelerates or decelerates charged particles as they enter the instrument which alters their deflection. A payload potential of -1 V adds 1 V of energy to an incident positively charged particle and decreases the energy of a negatively charged particle by the same amount. The incident energy of a 200 amu particle is 1 eV for a rocket velocity of 1000 m/s. Hence the payload potential has a significant effect on collection efficiency for masses of up to 200 amu but the effect is small for particles more massive than 2000 amu. The effect of the rocket payload potential (measured to be between -0.2 V and -1.5 V) on charged particles is included in the trajectory simulations by having the electric potential change by the measured amount above the entrance slit in a region approximately 1 Debye length in extent ($\sim$1 cm). The altitude dependence of these parameters is included in the calculations to find the collection efficiencies.

The ranges of mass collected for each electrode at each of the simulated altitudes are listed in Table 1. The electrodes are numbered 1–5 in order of increasing distance from the slit and thus in order of increasing particle mass. The nominal mass ranges for each electrode at 85 km are: (1) <500 amu, (2) 500–2000 amu, (3) 2000–8000 amu, (4) 8000–20,000 amu, and (5) $>50{,}000$ amu. The mass ranges for the positive charge collectors are approximately the same as for the negative charge collectors, except for electrode pair 1 which is most affected by the payload potential.

Fig. 5 shows the collection efficiencies for electrodes 2, 3, 4, and 5. The narrow gap in the range of collected mass just below 10^5 amu is from the air exit windows being located between electrode pairs 4 and 5. The heaviest particles, collected on electrode pair 5, are nearly undeflected and may be collected with equal probability by either of the two electrodes on the bottom (see Fig. 4); hence the efficiency of each of these electrodes approaches 50% for the highest mass particles. Fig. 6 shows the collection efficiencies at five altitudes for electrode 1 collecting positive particles and for electrode 1 collecting negative particles. The collection efficiency curves for electrode pair 1 show the greatest sensitivity to charging potential (more negative at higher altitudes) and to collisions (greater at lower altitudes). At 80 km and above, where the payload potential is approximately -1.5 V and collisions are infrequent, negative particles lighter than about 200 amu are repelled by the payload and are not collected. At 65 km, however, these particles do enter the instrument possibly as a result of being pushed by the more frequent collisions. In contrast, positive particles are accelerated toward the slit by the negative payload potential and electrode 1 for the collection of positive charge is sensitive to the lowest mass particles at all altitudes.

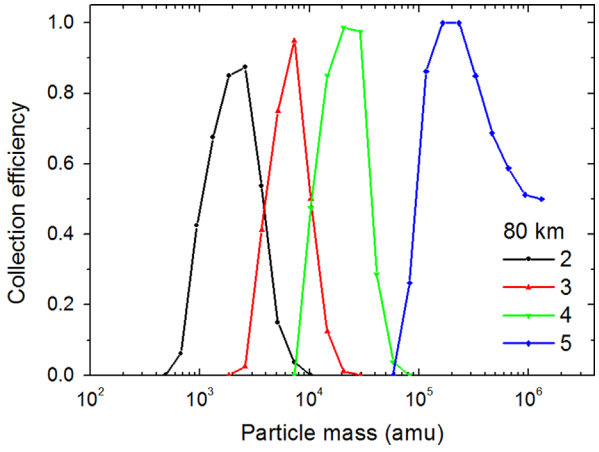

Fig. 5. Collection efficiencies for positively charged particles for electrodes 2, 3, 4, and 5 at 80 km. These curves are for a rocket velocity of 994 m/s and a measured payload potential of -1.4 V.

Table 1
Range of mass of particles collected by each MASS electrode at 65, 70, 75, 80, and 90 km. The mass limits given are the points where the collection efficiency has fallen to half the maximum. The mass ranges given without parentheses are for the positive electrodes. The ranges in parentheses are for the negative electrodes and are shown only where they are significantly different from the positive electrodes. For electrode 5, only the lower mass range is given.

Electrode	Mass at 65 km [amu]	Mass at 70 km [amu]	Mass at 75 km [amu]	Mass at 80 km [amu]	Mass at 90 km [amu]
1	<100	<200 (40–200)	<400 (160–400)	<1000 (300–1000)	100–900 (500–1400)
2	100–600	200–1600	400–2200	1000–4000	900–3000 (1500–4000)
3	600–4000	1300–5500	2000–6700	4000–10,000	3000–9500
4	3000–24,000	5000–26,000	6700–26,000	11,000–37,000	9500–26,000
5	$>23{,}000$	$>54{,}000$	$>80{,}000$	$>94{,}000$	$>84{,}000$

Please cite this article as: Robertson, S., et al., Detection of meteoric smoke particles in the mesosphere by a rocket-borne mass spectrometer. Journal of Atmospheric and Solar-Terrestrial Physics (2013), http://dx.doi.org/10.1016/j.jastp.2013.07.007

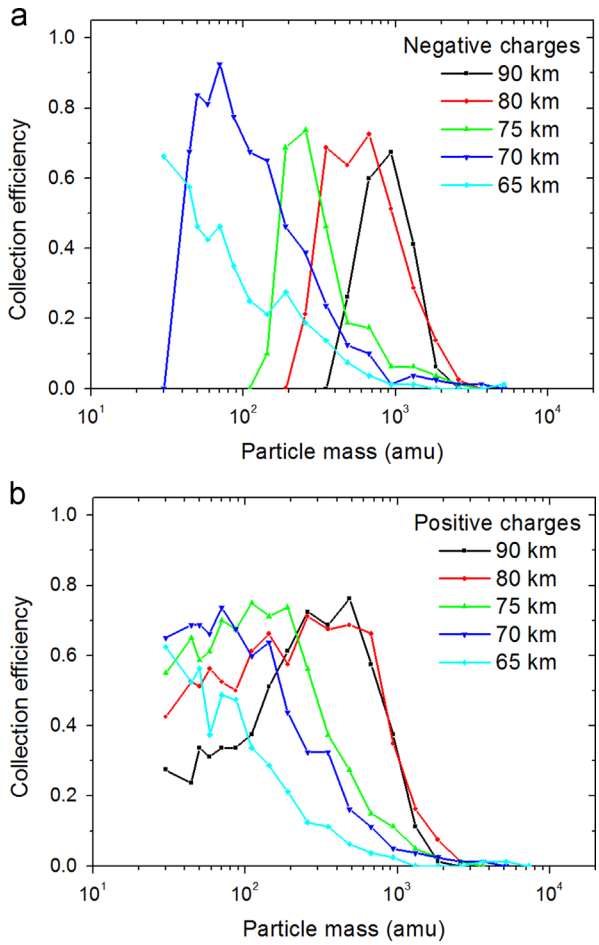

Fig. 6. Collection efficiency curves at five altitudes for (a) electrode 1 collecting negative particles and for (b) electrode 1 collecting positive particles. These curves show the effects of changes in rocket velocity, payload potential, and collision frequency.

2.1.3. Sources of spurious signals

There are two sources of spurious signals. The first is charge collection from ions entering the air exit windows. These windows are covered by screens biased by −9 V to prevent entry of ambient electrons which would make spurious signals much larger in magnitude. The ions entering the windows were observed as a spurious signal on the collectors for positive charge. The spurious signal is greatest for the collectors nearest to the exit windows and compromises the data only above 80 km where ions have a much greater number density. The second source of spurious charge is photoemission of electrons within the instrument. This spurious signal, seen only on the collectors for negative charge during the daytime, is discussed further in Section 3.3.

A possible source of spurious signals is secondary charge generation analogous to that seen from the impact of the icy NLC particles that can be tens of nanometers in radius (Havnes and Næsheim, 2007; Kassa et al., 2012). However, laboratory experiments with accelerators for nanometer-scale particles with compositions similar to MSPs have shown the absence of charge generation for these smaller particles moving at velocities typical of sounding rockets (Dalmann et al., 1977).

2.2. Colorado dust detectors

The payloads carried four Colorado Dust Detectors (CDD) (Robertson et al., 2004; Amyx et al., 2008) spaced 90° apart around the periphery of the forward bulkhead, Fig. 1. Each detector has a 7.2 cm^2 graphite surface that is connected to an electrometer which records the net current deposited by incident particles. The surface is tilted 15° from the payload axis so that the particles are incident obliquely. The collection of ambient electrons is reduced by a magnetic field from a permanent magnet placed behind the surface. Each CDD detector collects both positively and negatively charged MSPs and thus measures the net charge density for particles heavy enough to overcome aerodynamic drag at the payload shock front. Numerical simulations of similar impact detectors on different payloads (without the consideration of detector bias potentials) have shown that particles below about 1 nm in radius are carried past the surface by the air flow and are unlikely to be detected, with this size threshold higher at lower altitudes (Horányi et al., 1999; Amyx et al., 2008). The sensitivity of the CDD is also dependent upon the potential of the collecting surface, and there are not yet simulations for impact detectors which take this into consideration. A bias voltage of +2.5 V relative to the payload is used for two of the four collection surfaces (CDD pair 2) so that the lightest positive ions are repelled and so that any photoelectrons emitted from the surface during the daytime launch are returned. Having multiple CDDs on the payload, with both biased and unbiased surfaces, aids in the identification of ion signals and spurious photoelectron signals. An approximate net charge density is calculated using the impact area of the detector and the collected current. The CDDs have been used successfully to detect the larger particles responsible for NLC and PMSE (Smiley et al., 2003) and have detected MSPs in flights outside the NLC/PMSE season (Amyx et al., 2008). Comparison of CDD net charge density data with data from the MASS instrument aids in interpretation of data from both instruments and also in the interpretation of CDD data from other rocket campaigns.

2.3. Faraday rotation antennas

Antennas at the aft end of the payload were used to derive electron densities using the well-established Faraday rotation method. The technique makes use of the fact that the polarization of an electromagnetic wave rotates proportionally to the electron content between the transmitter and receiver (Mechtly et al., 1967; Bennett et al., 1972). The effect is generally more pronounced for lower frequencies; however, higher frequencies penetrate deeper into the ionosphere. Therefore, four frequencies are used for good overlap of the measurement ranges. The lowest frequency (1.3 MHz) is below the local electron gyro frequency in northern Scandinavia and provides the best unambiguous data in the presence of large collision frequencies at low altitudes (Jacobsen and Friedrich, 1979). The other sounding frequencies are 2.2, 3.883 and 7.835 MHz. The established magneto-ionic theory used for analysis is the one given by Sen and Wyller (1960), and a slightly improved version is given by Friedrich et al. (1991). The four transmitters (500 W each) were located near the launch site and the four receivers, fed by the same antenna, were at the aft end of the payload (Fig. 1). The spatial orientation of the wave polarization is found by the antenna spinning with the payload. The spin of this payload (2 Hz) led to four maxima and minima per second, i.e. whenever the antenna was parallel or perpendicular to the wave's polarization. Given the typical rocket velocity in the D-region (800 m/s), these extrema led to a height resolution of 200 m. The downleg data are considered inferior because the ray from the ground transmitter to the payload is oblique and conceivably deviates from a straight line.

2.4. Plasma probes

The four plasma probes (two positive ion probes and two Langmuir probes) were each placed at the end of a boom 60 cm in length (Fig. 1). The DSMC simulations showed that this length

Please cite this article as: Robertson, S., et al., Detection of meteoric smoke particles in the mesosphere by a rocket-borne mass spectrometer. Journal of Atmospheric and Solar-Terrestrial Physics (2013), http://dx.doi.org/10.1016/j.jastp.2013.07.007

places the probes well outside the shock wave that forms around the forward section (Fig. 3a).

2.4.1. Swept-bias Langmuir probe

The swept Langmuir probe has a cylindrical tip 3 mm in diameter and 50 mm long that is coated with colloidal graphite paint for a more uniform surface potential. The probe tip is swept in voltage (relative to the payload) from −4.5 V to +6.8 V in 34 ms and the return to −4.5 V is made in 23 ms. In order to reduce the duration of any disturbance to the payload potential, the sweeps are made at intervals of 200 ms. The probe is held at −4.5 V during the "resting" period between sweeps so that negligible current is drawn. Some interference from the probe sweeps was seen on other instruments in flight, but this was of brief duration (a few milliseconds) and only at the most positive voltage excursion of the probe. The probe voltage and current data are recorded at a 32 kHz rate, which provides collected current data at steps in bias voltage of approximately 0.01 V. There is an abrupt onset of electron collection when the probe tip passes the plasma potential. This onset point is found for each upsweep using a least-squares method to fit a baseline to the "resting" signal and a sloping line to the increasing current. The intersection of the lines is taken as the plasma potential. The payload potential relative to the plasma is the negative of the voltage found. All of the other electrically biased instruments are biased relative to the payload body, therefore, as the payload potential changes with altitude, so do instrument bias voltages relative to the ambient plasma. The payload potential measurement is thus used to aid in interpretation of the data from the other instruments.

2.4.2. Positive ion probes

The positive ion probes (PIP) consist of an inner solid sphere (8 mm in diameter) surrounded by a highly transparent grid (45 mm in diameter) which is fixed at the payload potential. One of the probes (LV) has the inner sphere electrically biased at −2.6 V and the other probe (HV) has a bias potential of −4.0 V (relative to the payload body). Ions that enter the grid are collected by the inner sphere, hence the ion density is simply related to the current measured and to the volume sampled by the gridded outer sphere. The contribution of the ions' thermal velocity to the collected current is only marginal and therefore an exact knowledge is not critical (Folkestad, 1970). The two different bias potentials were used to find if the more negative bias would collect more of the heavier smoke particles.

2.4.3. Fixed-bias Langmuir probe

The fixed-bias probe for ion collection is structurally nearly identical to the swept-bias probe and was mounted 180° from the swept-bias probe to rotationally balance the payload. The data serve only as a secondary indicator of the abundance of positive ions. The fixed-bias Langmuir probe has a cylindrical tip 12.5 mm in diameter and 50 mm long that is painted with colloidal graphite to create a uniform surface potential. The bias potential is −3.6 V relative to the payload potential so that the probe collects ions. The collisionless version of the orbit-motion-limited theory of probes (Hershkowitz, 1989) fails to apply because of the varying speed of the supersonic payload and the varying ion-neutral collision frequency which determines the ion mobility. Hence the data are presented as a collected current rather than an ion density because of their uncertain relationship.

2.5. Photoemission instruments

In the 2007 flights of the MASS instrument in daylight (Robertson et al., 2009), part of the collected current was attributed to photoemission within the instrument rather than from collection of charged aerosol particles. In order to gauge the importance of this effect for the daytime CHAMPS flight, a set of photoemission instruments was included in the aft section of the payload. One of these instruments is an aluminum disk (to represent the material of the payload body) 20 mm in diameter placed behind a highly transparent grid that is grounded to the payload body. The disk is biased to −9 V so that photoelectrons emitted from the surface are collected by the grid. The photoemission current is measured by an electrometer.

2.6. Ground-based lidar

Lidar was used to verify that temperatures in the mesosphere were sufficiently high to preclude the existence of ice particles. The data were taken at the Arctic Lidar Observatory for Middle Atmospheric Research (ALOMAR) which is collocated with the Andøya Rocket Range launch site. The lidar transmits at three wavelengths in the sodium resonance fluorescence D2a line (589 nm) to measure the Doppler shift and Doppler broadening of the atomic sodium layer near the mesopause. The lidar measures Na density from 80 to 105 km and temperature and radial wind from ~82 to 100 km. Measurements can be made using one or two beams during both day and night. The lidar was installed in July 2000 and it has supported many rocket campaigns, including Winter and Summer MacWAVE, DELTA I and II, and ECOMA/MASS (Williams et al., 2006a, 2006b).

3. Data

The two CHAMPS rockets were launched in October, 2011, from the Andøya Rocket Range (69°N, 16°E), Norway, after the end of the NLC/PMSE season in order to have a sufficiently "warm" mesosphere to prevent the detection of ice particles. Bremer et al. (2003) place the NLC season between 8 June and 13 August and the PMSE season between 19 May and 28 August. The night launch (designated 41.094) was 11 October at 21:50 UT and had an apogee of 125 km and a solar zenith angle of 117.3°. The day launch (designated 41.093) was 13 October at 13:50 UT with an apogee of 117 km and a solar zenith angle of 83.5°. For both launches, data collection began near an altitude of 65 km, after ejection of the nosecone and aft skirt, and continued on the downleg to 60 km.

For an altitude of 80 km, the downleg data correspond to a position displaced ~70 km horizontally from the upleg data location at an azimuth of 330°. For the daytime flight, the data recorded by all instruments are nearly the same for the upleg and downleg. For the nighttime flight, however, measured particle and ion densities are higher on the upleg than on the downleg (this behavior is seen by all instruments). Additionally on the nighttime flight, the ion and MSP density profiles appear to be shifted to a higher altitude by ~5 km on the downleg. Data from the upleg of each flight are used for detailed analysis due to the available electron density measurements from the upleg Faraday rotation measurements, but data from both legs of each flight are shown for completion.

3.1. Lidar data

The Na lidar obtained data for the nighttime launch on 11 October 2011 despite intermittent cloud coverage, Fig. 7. Two beams were used, one at 20° north of zenith (~9 km east of the rocket upleg position at 85 km altitude) and one at zenith (~27 km SSE of the rocket upleg position at 85 km altitude). The temperature profiles in both beams are similar; hence we plot only

Please cite this article as: Robertson, S., et al., Detection of meteoric smoke particles in the mesosphere by a rocket-borne mass spectrometer. Journal of Atmospheric and Solar-Terrestrial Physics (2013), http://dx.doi.org/10.1016/j.jastp.2013.07.007

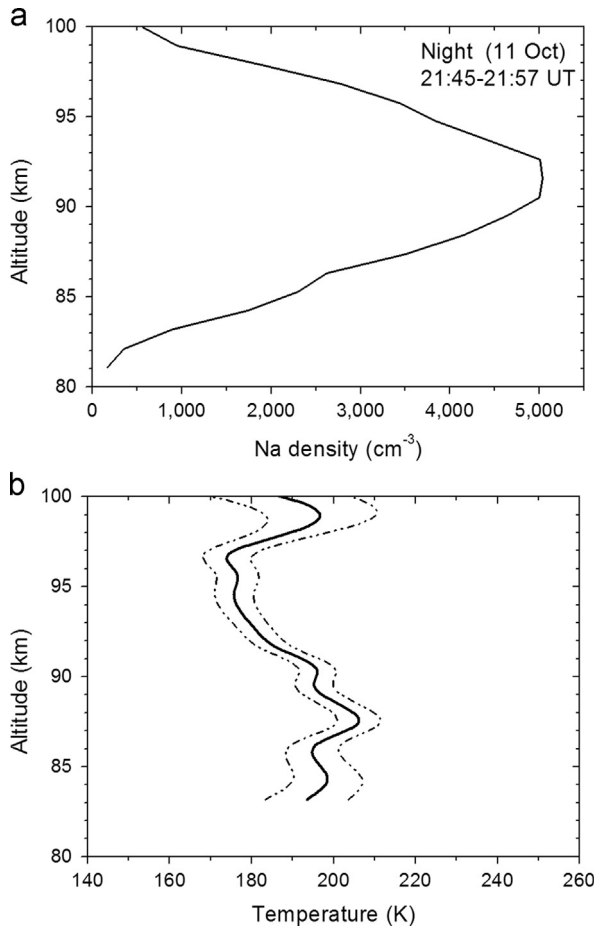

Fig. 7. (a) Sodium density and (b) temperature from the ALOMAR lidar for the 11 October nighttime launch. The data are integrated for an interval spanning the launch time. The error range in the temperature data is indicated by the dashed lines.

the zenith beam averages from 21:45 to 21:57 UT. The temperature decreases from ~200 K at 85 km to ~175 K at 95 km. The vertical wind (not shown) is near zero on average, as expected, with a wave of short vertical wavelength visible in the vertical wind, temperature, and Na density. There is nothing unusual in either the mesopause mean state or dynamics for this night. For the daytime launch on 13 October, there were clouds at the time of the launch; however, limited lidar data were obtained with the zenith pointing beam 3 h afterward from 17:02 to 17:06 UT, Fig. 8. Temperatures range from 240 K at 85 km to 180 K at 95 km, with a large gradient likely due to wave activity that is not averaged out by the short integration time. Otherwise, the data are typical and there is nothing unusual for this day.

The altitude range of the Na layer for both launches is nominal and extends from ~80 to 105 km with a peak near 92 km in the nighttime data and 86 km in the daytime data. Studies of NLC have shown that the icy NLC particles occur when the temperature falls below 154 K (Lübken et al., 1996), with even lower temperatures needed at higher altitudes. The measured temperature profiles for both launches show that the atmosphere was insufficiently cold for the formation and growth of ice particles; hence any observed aerosol particles must be meteoric smoke particles and not ice.

3.2. Plasma data

3.2.1. Electron density from Faraday rotation

The electron densities, Fig. 9, were deduced from the Faraday rotation data taken on the uplegs of the flights. The nighttime data show that the electron density above 75 km was higher than for the daytime launch indicating increased ionization from energetic particles (direct solar ultraviolet being absent). The nighttime data show a sharp decrease in electron density below the D-region ledge near 82–24 km. The nighttime decrease is usually attributed to electron attachment (Friedrich et al., 2012) and is confirmed by data from the MASS instrument which detected increased light negative charges below 80 km.

3.2.2. Positive ion data

The positive ion probe data, Fig. 10, have been converted to number densities using a scale factor that makes the electron and ion densities equal near apogee. In the nighttime data, the LV and HV probe data show nearly the same density above 80 km, but at lower altitudes the HV probe collected more charge. This difference is likely due to the occurrence of heavy charge carriers that are collected by the higher bias potential but not the lower. This interpretation is supported by the data from the MASS instrument which shows an onset of positive charge collection below 80 km for particles in the 500–2000 amu mass range. In the daytime data, the HV probe signal is both above and below the LV probe, indicating a malfunction or more likely a spurious signal associated with daytime conditions such as photoemission. The data plotted are an average of the LV and HV data.

The data from the fixed-bias Langmuir probe collecting ions, Fig. 11, shows the collected current generally increasing with altitude on both flights. Some of the high altitude data are missing because the electronics were saturated. The daytime ion data for both the PIP and the fixed-bias Langmuir probe show the ledge at 84 km seen in the electron density by the Faraday rotation antennas that is usually assumed to be the boundary below which there are significant numbers of cluster ions.

3.2.3. Payload potential from swept Langmuir probe data

The payload potential deduced from the swept probe data is shown in Fig. 12 for both flights. For the upleg of the night launch there is an abrupt transition from −0.25 V below 67 km to about −1.6 V above that altitude. The less negative potential at the lower altitudes is attributed to the lower electron density at the lower altitudes. The daytime time data show potentials typically in the range −1 V to −2 V. The more negative payload potential at the lower altitudes in the daytime is likely a consequence of the higher electron density at low altitudes during the day than at night.

3.3. Photoemission data

Fig. 13 shows the data from the aluminum photoemission detector on the daytime flight. The data are plotted as lines connecting points which are the peak photoemission on each rotation that occurs when the aluminum emitting surface is facing most sunward. There is a very small signal when facing away from the sun that increases with altitude and is likely from collection of ions passing through the grid. The photoemission observed on the upleg is thought to be greater than that on the downleg as a result of evaporation of water vapor and other contaminants on the surface that increase the emissivity. These data show photoemission increases by about an order of magnitude from 80 to 90 km, and this helps to identify spurious signals from photoemission within the MASS instrument. Photoemission is not detected on the night flight.

3.4. Colorado dust detector data

Two of the four CDD on each flight had detector surfaces biased to +2.5 V relative to the payload in order to repel positive ions. The payload potential was approximately −1.5 V so that the detectors

Please cite this article as: Robertson, S., et al., Detection of meteoric smoke particles in the mesosphere by a rocket-borne mass spectrometer. Journal of Atmospheric and Solar-Terrestrial Physics (2013), http://dx.doi.org/10.1016/j.jastp.2013.07.007

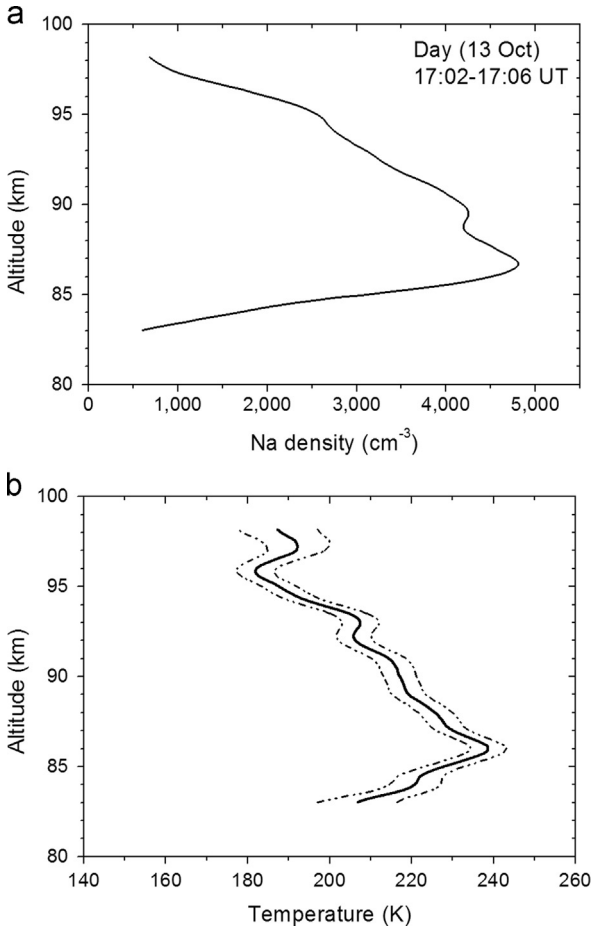

Fig. 8. (a) Sodium density and (b) temperature from the ALOMAR lidar for 13 October approximately 3 h after the daytime launch.

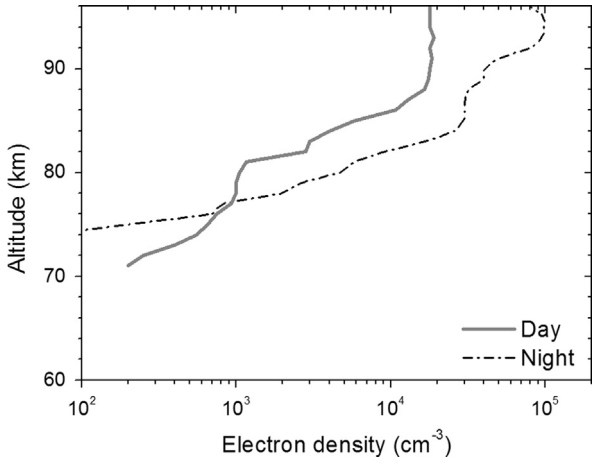

Fig. 9. Electron density for the two flights from Faraday rotation measurements (upleg data).

fixed at the payload potential (CDD pair 1) were effectively negatively biased to about −1.5 V relative to the ambient plasma, and the positively biased detectors (CDD pair 2) were effectively biased to +1 V relative to the plasma. Given the 15° tilt of the detector surface relative to the payload axis, the positive bias potential is sufficiently strong to prevent detection of positively charged particles of less than ~750 amu. Therefore, any nearly identical signals detected by both pairs of CDDs are due to dust particles at least heavier than this mass, and differences between CDD1 and CDD2 data are due to differing collections of lower mass dust particles and ions.

CDD data from the nighttime upleg and daytime upleg are plotted in Fig. 14. For both flights, the signal from the positively biased CDD2 returns to near zero at 80–85 km while the signal from the negatively biased CDD1 continues to sharply increase. A similarly increasing signal is seen in the positive ion probe data. These data indicate that on both flights the unbiased dust detectors were collecting positive ions (in addition to MSPs) at altitudes above ~75 km. Below this altitude, the biased and unbiased CDDs observe approximately the same signals, indicating that the signals are due to MSPs.

For the nighttime flight, the biased and unbiased CDDs detected two net positive peaks in charged MSPs below ~75 km with maximum recorded densities occurring near 73 km and 63 km. The data from the negatively biased CDD1 suggests a net negatively charged heavy dust layer extending from 82 to 94 km. For the daytime flight, the positively biased CDD2 collected photoelectrons emitted by the surrounding payload while the negatively biased CDD1 emitted photoelectrons from the detector surface, causing the signals to go off scale in different directions at the highest altitudes. Maximum photoemission signals occurred when the surfaces were facing the sun. Effects of photoemission were minimized in the data by plotting only the maximum and minimum signal per rotation for the CDD2 and CDD1 data, respectively. Both biased and unbiased CDDs see a single net positive dust layer below 75 km during the day. It is possible that more negatively charged dust was present below ~70 km than was detected by the CDDs due to a particularly high negative payload potential at these altitudes that likely repelled the negative MSPs.

3.5. MASS data

The order of presentation of the data from the MASS instrument is as follows. The data from electrode pair 5 are presented first to show the altitudes at which spurious charge collection from ambient ions occurs. The data from electrodes 2, 3, and 4 recording MSPs are presented second. The data from electrodes 1 recording both ions and less massive MSPs are presented third, using the results from electrodes 2, 3, and 4 to assist in determining the origin of the signals. The daytime data are presented after the nighttime data because the daytime data are more difficult to interpret.

3.5.1. Spurious ion signals

The electrode pair 5, located at the bottom of the instrument below the windows, was designed to collect the heaviest particles that are not deflected onto any of the first four electrode pairs (Fig. 4). Simulations showed that these weakly deflected particles would have masses greater than ~50,000 amu. Ice particles in this mass range were detected in the 2007 flights into NLC, but the MSPs examined by the CHAMPS flights are not expected to grow to this size. This pair of electrodes showed no signal other than occasional spiky signals (due to operation of the attitude control system) below 80 km where MSPs were observed on the other electrodes. Therefore, the fifth pair of electrodes served primarily to indicate when the instrument was affected by ions entering through the exit windows (discussed in Section 2.1.3). These electrodes showed positive charge collection above ~88 km on the night flight, Fig. 15, and above ~92 km on the day flight (not shown) which is consistent with the ion signals detected by the PIPs and negatively biased CDD1. The fourth pair of electrodes recording masses 8000–20,000 amu is adjacent to the top edge of the exit windows and showed this spurious ion collection as well.

Please cite this article as: Robertson, S., et al., Detection of meteoric smoke particles in the mesosphere by a rocket-borne mass spectrometer. Journal of Atmospheric and Solar-Terrestrial Physics (2013), http://dx.doi.org/10.1016/j.jastp.2013.07.007

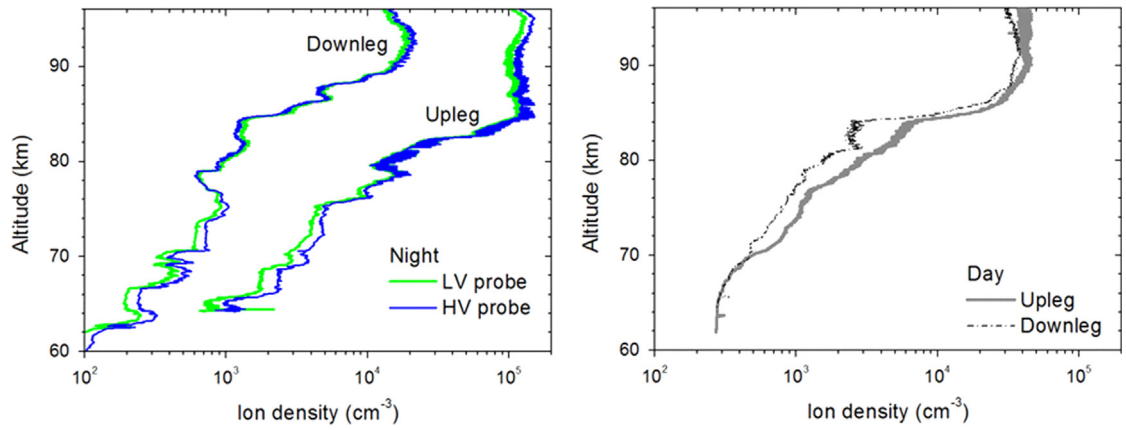

Fig. 10. Ion densities deduced from the PIP probes for each flight. For the nighttime flight, the HV probe has a higher bias voltage than the LV probe resulting in a slightly greater collection of current. For the daytime flight, the LV and HV probes have been averaged.

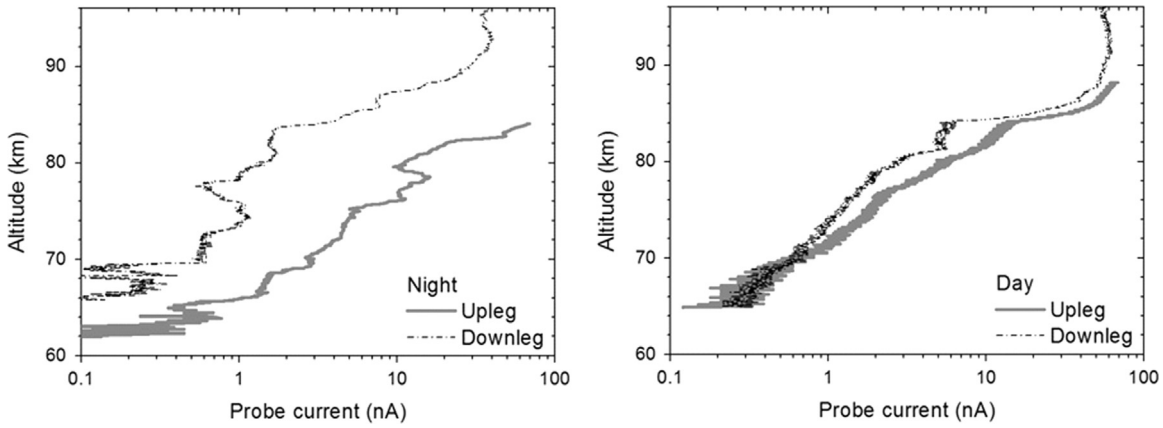

Fig. 11. Collected current by the Langmuir probe biased to collections for each flight. The signal was off scale for part of the flight durations on the uplegs. The data are smoothed with a median filter spanning 80 ms. The nighttime data from the Langmuir probes and PIPs show a profile shifted ~5 km upward on the downleg.

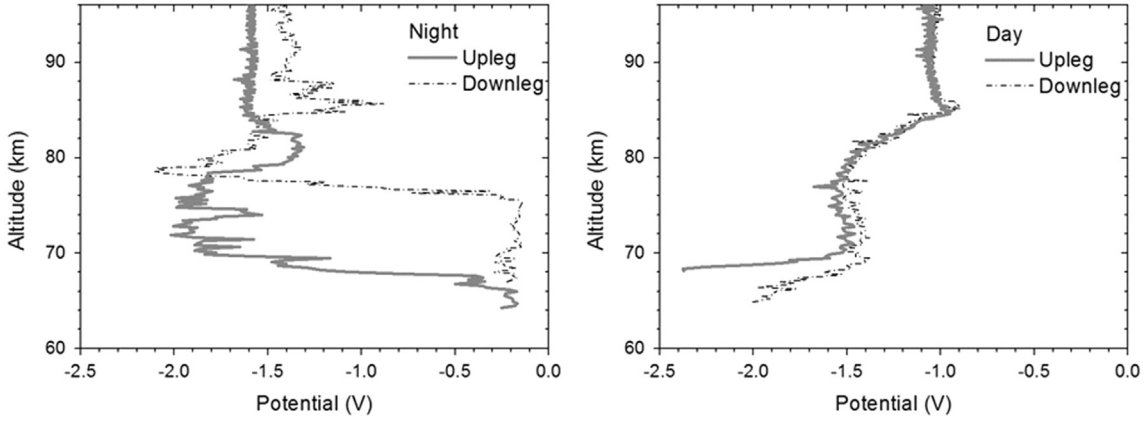

Fig. 12. Potential of the payload from the swept Langmuir probe data for each flight. The data are not plotted for the lowest altitudes because there is insufficient current collection for analysis.

3.5.2. Nighttime MSPs, 500–20,000 amu

The data for electrode pairs 2, 3, and 4 are shown in Fig. 16. For the nighttime flight, the number density profiles are similar on the upleg and downleg, however, the densities are reduced by about 50% on the downleg (similar to the density reductions seen by the plasma instruments). The data show positively and negatively charged MSPs below 80 km with masses in the ranges 500–8000 amu, with the higher masses occurring at lower altitudes. At higher altitudes, there are only negatively charged MSPs.

For positively charged MSPs, the 500–2000 amu data show a maximum in number density of about 2500 cm^{-3} on the upleg at 70 km. Below 70 km, the density falls gradually to about 1000 cm^{-3} at 60 km. If the MSPs are in a layer, the lower limit of the layer is below 60 km, the lowest altitude from which data were returned. Above 70 km, the density falls to below 10 cm^{-3} at 78 km. There is some modulation of the number density by wave activity having a vertical wavelength of a few kilometers, as is seen in the lidar data. The 2000–8000 amu data show significant

Please cite this article as: Robertson, S., et al., Detection of meteoric smoke particles in the mesosphere by a rocket-borne mass spectrometer. Journal of Atmospheric and Solar-Terrestrial Physics (2013), http://dx.doi.org/10.1016/j.jastp.2013.07.007

numbers of particles only below 66 km, with the values up to 700 cm^{-3} on the upleg. The lower altitude for the onset of the heavier particles is probably due to growth by coagulation during sedimentation. The 8000–20,000 amu electrode recorded only noise below 80 km, indicating negligible numbers ($<10\ cm^{-3}$) of these particles below this altitude.

Above 82 km there are spurious signals (shown as dotted lines) arising from the positive ions that enter through the exit windows. The origin of this spurious signal was identified in Section 3.5.1 above. Modeling has shown that rapid sedimentation prevents significant numbers of MSPs at and above 95 km. As a consequence of the largest bias voltage being on electrode 4, it collected nearly all of the positive ions moving upward from the windows (beginning at an altitude of ~82 km) and electrodes 1 through 3 were therefore much less affected. These charges admitted through the windows do not follow the paths used for the collection efficiency curves and consequently the mass identification for the channels is meaningless for the spurious signal.

For negatively charged MSPs, the data are similar to those for the positively charged MSPs below about 75 km. The 500–2000 amu particles have a plateau of ~2000 cm^{-3} below 70 km on the upleg that is similar to the behavior seen in the positively charged particles. The 2000–8000 amu particle density rises above 10 cm^{-3} below 68 km, an onset also seen in the positively charged particles. The data above 80 km for negative MSPs shows what appears to be a layer with a lower boundary at 75 km and an upper boundary at 94 km. In this altitude range, the positive charge collectors are affected by positive ions entering the exit window; however, the negative charge collecting electrodes are not sensitive to these ions as a consequence of their positive bias voltages. The data in the 500–2000 amu and the 2000–8000 amu ranges which have a local maximum of 200 cm^{-3} at 85 km are true signals from negatively charged MSPs. The signal from the 8000–20,000 amu electrode (adjacent to the air exit window) continues to increase above 90 km where these larger MSPs are not expected likely due to collection of ambient electrons.

3.5.3. Nighttime MSPs and ions, 0–500 amu

The data collected by the first pair of electrodes is discussed separately because it includes detection of the lightest MSPs and ions. The nighttime data from the first pair of electrodes are shown in Fig. 17. Both the positive and negative charge data show features seen by electrodes 2 and 3 such as positive and negative charge densities increasing below 80 km and the occurrence of the higher altitude negative charge layer. However, because the electrode 1 signals also include ions that cannot be distinguished from MSPs, the charged MSP number densities for this mass range can only be estimated by excluding the smooth increase attributed to the ions alone.

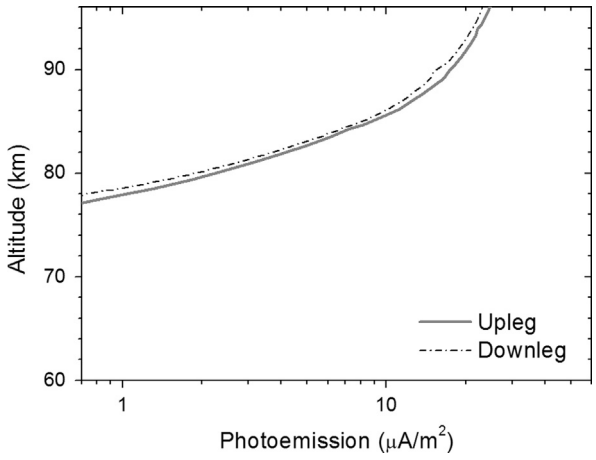

Fig. 13. Photoemission from an aluminum surface for the daytime flight. The lines connect the data points that are the peak emission on each rotation of the payload.

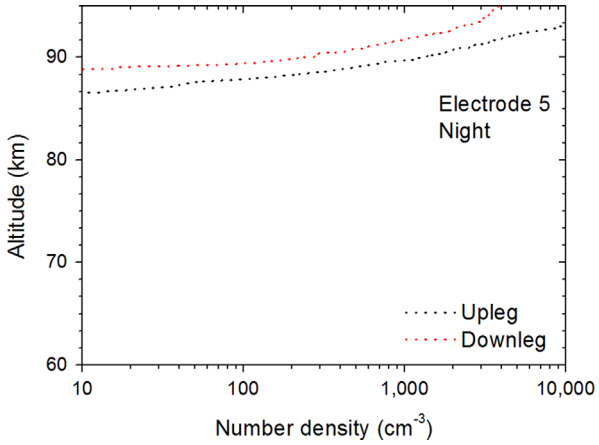

Fig. 15. Signal from the mass spectrometer's electrode 5 designed to collect positive charge from masses greater than 50,000 amu. The observed signal is a spurious signal from ions entering the air exit windows. The signal has been converted to an equivalent charge density for comparison with other data plots. Signals from spurious charge are indicated in the plots by dotted lines.

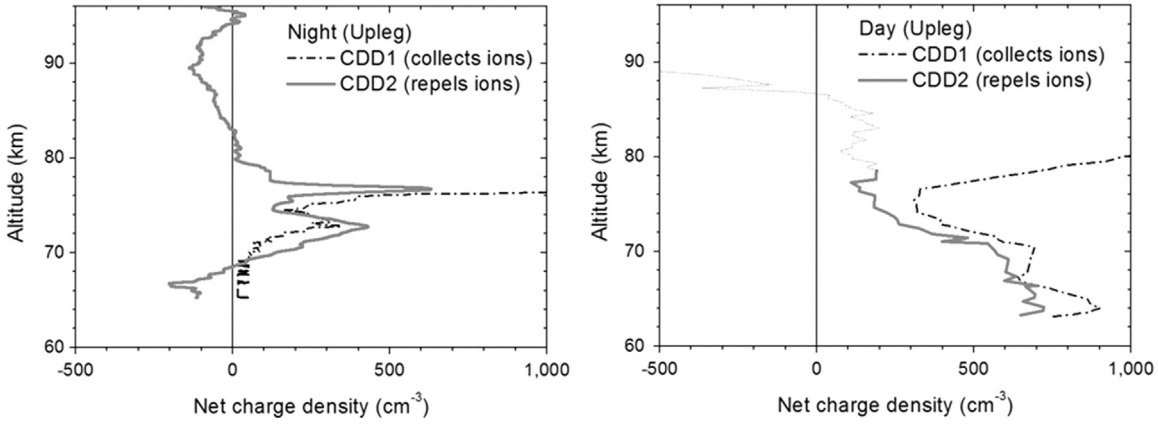

Fig. 14. CDD data for each flight (upleg only). The signals below 76 km are similar, indicating distinct net positive dust layers. Above 76 km, CDD1, which does not have the positive bias voltage, shows an increasing signal from positive ions not seen in the data from CDD2, which is positively biased.

Please cite this article as: Robertson, S., et al., Detection of meteoric smoke particles in the mesosphere by a rocket-borne mass spectrometer. Journal of Atmospheric and Solar-Terrestrial Physics (2013), http://dx.doi.org/10.1016/j.jastp.2013.07.007

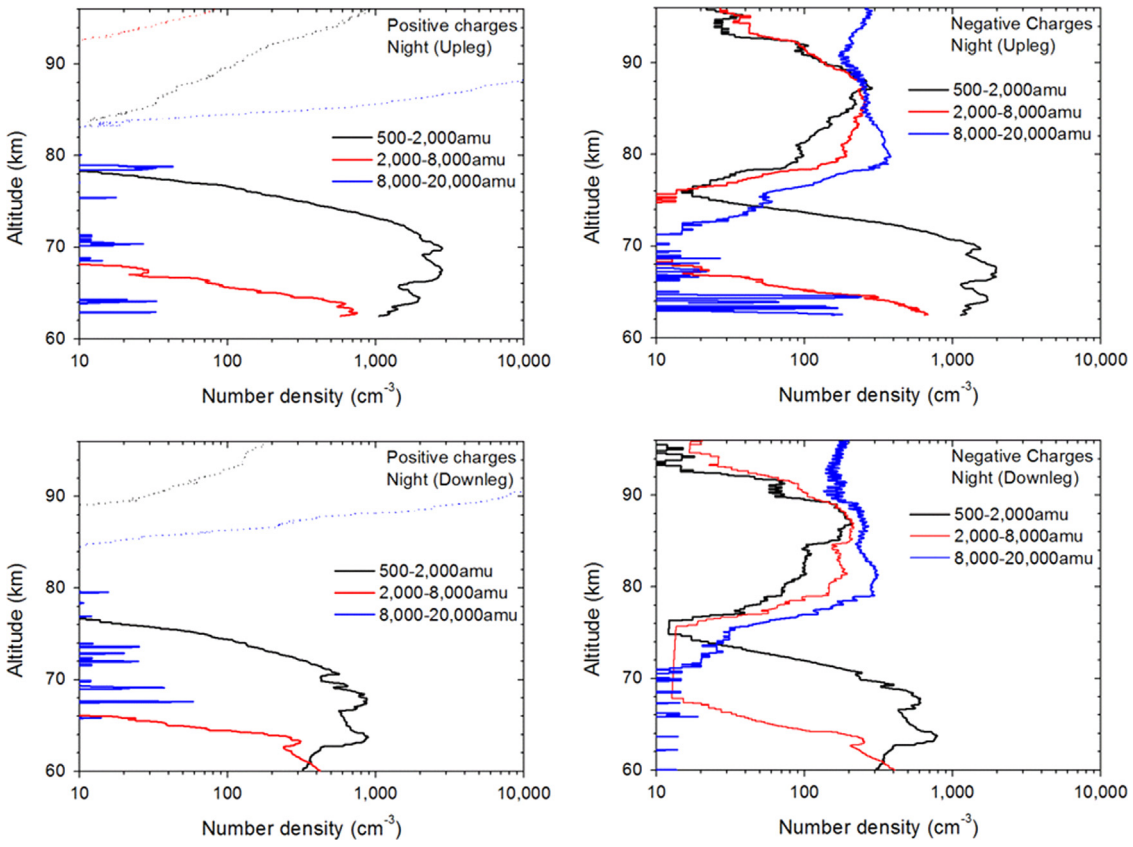

Fig. 16. Measured nighttime number densities of positively and negatively charged particles for the center three electrodes (2–4) of the mass spectrometer. Dotted lines in figures indicate data that are likely due to spurious charges. The upleg data begin at 62.5 km, following nosecone ejection.

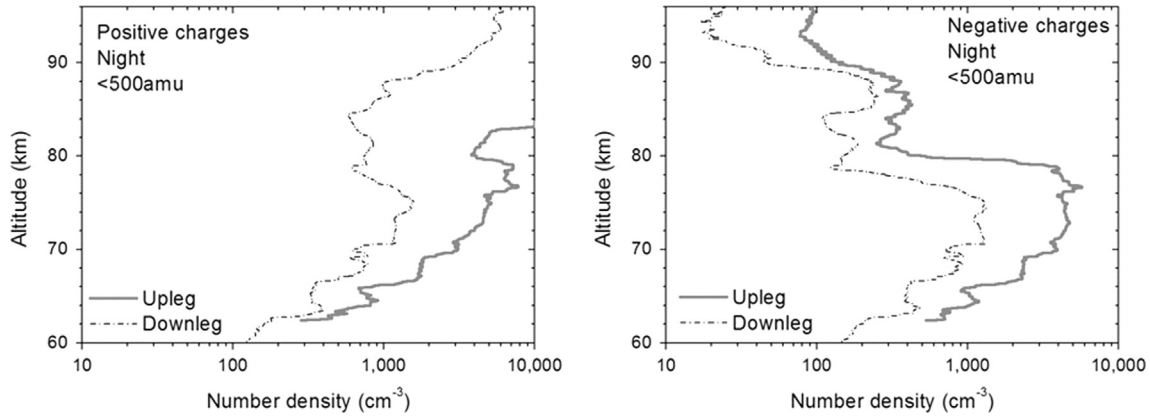

Fig. 17. Measured number densities of positively and negatively charged particles for the first pair of spectrometer electrodes nominally collecting 0–500 amu which includes both ions and MSPs. The detected range of mass varies with altitude (Table 1). Electrons are excluded from collection by the payload potential.

The electrode collecting positive charges shows a signal generally increasing with altitude that is consistent with the increasing density of positive ions seen in the data from the PIP, fixed-bias Langmuir probe, and the negatively biased CDD1. There is a stepwise increase just below 80 km that coincides approximately with the onset of collection of positive MSPs in the 500–2000 amu mass range. The increase by $\sim$2000 cm^{-3} seen in the 0–500 amu data at this altitude may therefore indicate a positively charged MSP layer superimposed on the ion background. A similar feature at 78 km is seen in the nighttime PIP data and in all CDD data, further indicating the presence of charged particles more massive than molecular ions.

The first electrode collecting negative charge was affected by the changing payload potential which shifts the nominal mass collection range from 0–500 amu to 160–400 amu at 75 km (Table 1). This electrode was less sensitive to lighter particles above this altitude, and was more sensitive below. This changing sensitivity further complicates the assignment of data signals to ions or MSPs for the negative collector. The three negative ions thought to be most abundant are NO_3^-, HCO_3^-, and CO_3^-, with masses 61 ± 2 amu (Thomas and Bowman, 1985). The numerical simulations for particle trajectories indicated that these masses were excluded from collection due to the payload potential at 75 km and above which suggests that the upper charge layer is primarily due to MSPs.

The upleg signal for negative charges of 160–400 amu indicates a peak density of $\sim$5000 cm^{-3} at 75 km, with a general decrease from this maximum for higher and lower altitudes (with a shallow minimum near 80 km). It is likely that these low mass negative charge signals are due to both MSPs and negative ions. MSPs appear

Please cite this article as: Robertson, S., et al., Detection of meteoric smoke particles in the mesosphere by a rocket-borne mass spectrometer. Journal of Atmospheric and Solar-Terrestrial Physics (2013), http://dx.doi.org/10.1016/j.jastp.2013.07.007

in the adjacent 500–2000 amu channel for altitudes below about 77 km. Therefore, it is reasonable to conclude that the $\sim$2000 cm^{-3} increase in density observed by electrode 1 below 80 km is at least partially due to MSPs with the higher altitude of the onset being due to the lower mass. The fraction of the signal arising from negative ions cannot be determined from the data.

Charge neutrality is examined for the nighttime flight by comparing the total density of positively charged particles with the total density of negatively charged particles. The MASS data are used for the densities of ions and MSPs and the Faraday rotation data are used for the density of free electrons. The total charge densities as well as the contributions from charged particles $>$500 amu alone are shown in Fig. 18. The densities are nearly equal for positive and negative charge below 80 km consistent with nearly all charges being detected. Above 80 km, the general shape of the altitude profiles for total positive and negative charge densities is similar; the positive charge densities are likely lower due to the reduced collection efficiency of positive particles less than 200 amu at these altitudes. Fig. 18 also shows that positively and negatively charged MSPs of $>$500 amu approximately coexist below 65 km, negative MSPs are dominant between 65 and 75 km, and only negatively charged MSPs occur between 75 and 95 km. The net charge data from the CDDs also indicate a net negative charge layer from 80 to 95 km. In contrast to the MASS data, however, the CDDs detected a net positively charged layer below this altitude. This suggests that at these altitudes the CDDs are not sensitive to the smallest negative MSPs.

3.5.4. Daytime MSPs, 500–20,000 amu

The daytime data for electrode pairs 2, 3, and 4 are shown in Fig. 19. The data from the upleg and downleg are nearly identical. The daytime data for positive MSPs show the same altitude profile for each of the electrodes as during the night, except with lower peak densities. As in the nighttime data, the daytime data show the 500–2000 amu particle density rising above 10 cm^{-3} below about 75 km; however, the peak density is $\sim$250 cm^{-3} rather than $\sim$2000 cm^{-3}. The data for the 2000–8000 amu electrode rises at about 65 km and also to a smaller value than at night. At higher altitudes, the data show the spurious signal from ions entering the exit windows that was identified in the nighttime data.

Interpretation of the daytime data for negative charges requires consideration of photoemission as a source of spurious negative charge. Solar ultraviolet illumination causes electron emission from the aluminum surfaces within the instrument. These electrons are collected on the electrodes biased to collect negative particles.

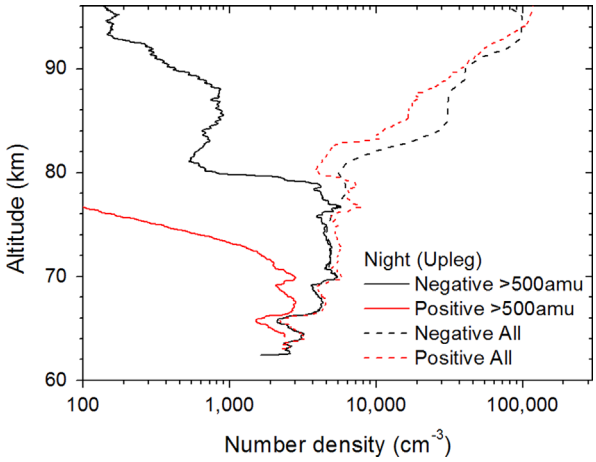

Fig. 18. Total positive and negative charge density observed on the nighttime flight (upleg only). The dust and ion signals are taken from MASS electrode pairs 1–4 data and the electron density is taken from Faraday rotation data.

The photoelectron signal in the MASS data is modulated at the rocket spin rate. This modulation has been removed by plotting only the minima (the data with the least contribution from photoemission). The daytime data for electrodes 2–4 show collection of negative charges that generally increases with altitude. The data do not show the expected decrease at the highest altitudes where MSPs are expected to be absent. This steady increase must be a consequence of the collection of photoelectrons since the altitude dependence is similar to that of the signal on the photoemission detector (Fig. 13). As expected, there is no signal corresponding to effects of photoemission in the data for positive charge collection.

In interpreting the daytime data for negative MSPs, we assume that the general trend is from increasing photoemission within the instrument and that deviations from this trend are due to collections of charged MSPs. There is a weak layer of negatively charged MSPs with number density $\sim$100 cm^{-3} at 81–87 km that is superimposed on the photoemission signal. This layer is seen on both the 500–2000 amu data and the 2000–8000 amu data. Similarly, the nighttime data show a layer at 78–93 km in the negatively charged particles which is attributed to a greater charged fraction as a consequence of the greater electron density. The daytime electrode 2 and 3 data also show a small signal for altitudes below $\sim$65 km that is much weaker than was seen in the nighttime data. Modeling has shown that the density of negatively charged MSPs can be reduced in the daytime by photodetachment (Klumov et al., 2000, 2005; Rapp, 2009; Knappmiller et al., 2011).

3.5.5. Daytime MSPs and ions, 0–500 amu

The 0–500 amu data for positive charges, Fig. 20, does not show any obvious layers and is consistent with the detection of molecular ions seen by the PIPs and negatively biased CDDs. The 0–500 amu data for negative charge shows a continuous increase from 65 to 95 km that is probably from collection of photoelectrons in addition to MSPs. There is an increasing density of negative MSPs and ions below 65 km. This signal is also seen in the 500–2000 and 2000–8000 amu data that are identified as MSPs, suggesting that the negative charges are MSPs rather than ions. The large number density of negative particles at 0–500 amu seen in the nighttime data (4000 cm^{-3} at 70–80 km) is missing in the daytime data. The Thomas and Bowman (1985) model shows fewer negative ions in daytime conditions.

Due to the significant effect of spurious signals from photoelectron detection, net charge densities and preservation of charge neutrality is not examined for the daytime flight. Correlation of the MASS dust signals with those detected by the CDDs is difficult for the same reason. The CDD data suggests nearly equal abundance of positively and negatively charged particles with a slightly positive excess. The MASS data may also suggest a net positive layer if the data from electrodes 1 and 4 which may include ions and photoelectrons, respectively, are not included.

4. Modeling

4.1. Particle charging model

The uncharged fraction of MSPs is not measured by the spectrometer; however, a charging model can be used to estimate this fraction. The charging model used here is the one presented in detail by Rapp and Lübken (2001) in which the rate coefficients for charging of MSPs are taken from an aerosol particle charging model for spherical particles (Natanson, 1960). The charging model has been simplified by assuming a single size of particle. The recombination of positive and negative MSPs is assumed negligible and no role is given to atomic oxygen or negative ions.

The adjustable inputs to the charging model are the ionization rate Q and the total number density of MSPs. The MSPs are allowed

Please cite this article as: Robertson, S., et al., Detection of meteoric smoke particles in the mesosphere by a rocket-borne mass spectrometer. Journal of Atmospheric and Solar-Terrestrial Physics (2013), http://dx.doi.org/10.1016/j.jastp.2013.07.007

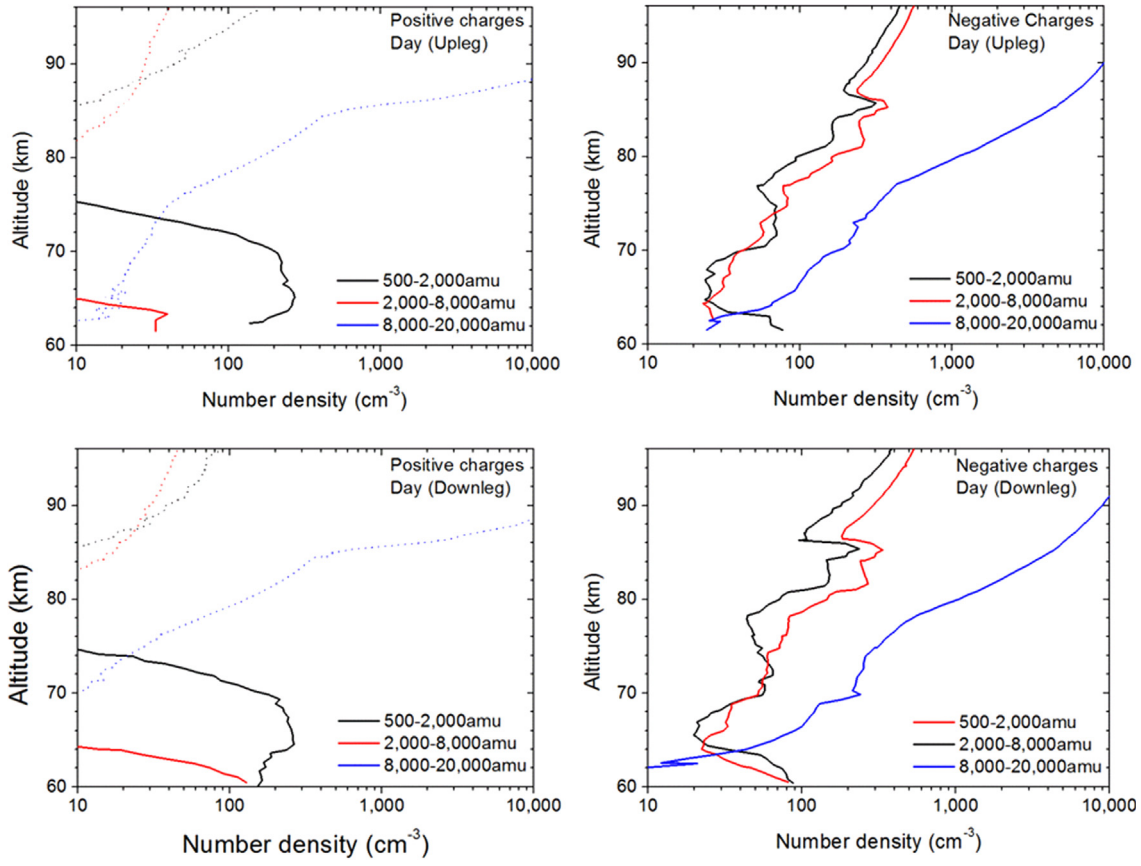

Fig. 19. Measured daytime number densities of positively and negatively charged particles for the center three electrodes (2–4) of the mass spectrometer.

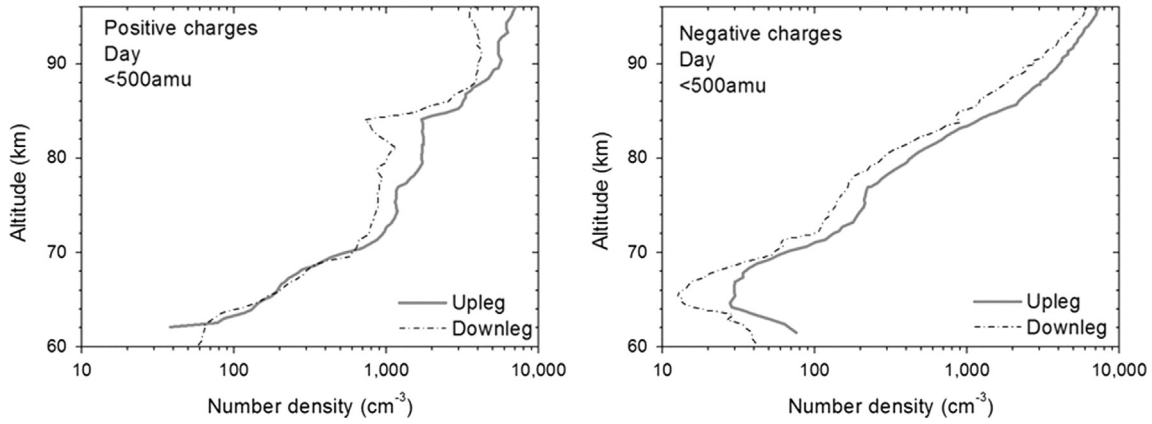

Fig. 20. Measured number densities of positively and negatively charged particles for the first pair of spectrometer electrodes nominally collecting 0–500 amu which includes both ions and MSPs. The signals for negative charge include photoelectrons from within the instrument. Dotted lines indicate data that are likely due to spurious charges.

to have charge numbers $Z=+1$, 0, and -1. The rate coefficients for the creation of MSPs with two charges are negligibly small for particles of order 1 nm in radius; hence multiply charged particles are ignored. The outputs of the model are the number density of electrons n_e, the number density of ions n_i, and the number densities $N(Z)$ of MSPs of charge state Z. The rate equations for the electron and ion number densities are

$$\frac{d}{dt}n_e = Q - \alpha_{ie} n_e n_i - n_e \sum_Z \alpha_e(Z) N(Z),$$

$$\frac{d}{dt}n_i = Q - \alpha_{ie} n_e n_i - n_i \sum_Z \alpha_i(Z) N(Z),$$

where α_{ie} is the electron–ion recombination rate coefficient, $\alpha_e(Z)$ is the rate coefficient for attachment of electrons to MSPs with charge number Z, and $\alpha_i(Z)$ is the same coefficient for ion attachment. The rate coefficients $\alpha_e(Z)$ and $\alpha_i(Z)$ are calculated from Natanson's formulas using 200 K as the electron and ion temperatures and 30 amu as the ion mass. The rate equations for MSPs of charge number Z are

$$\frac{d}{dt}N(Z) = \alpha_i(Z-1)N(Z-1)n_i - [\alpha_e(Z)n_e + \alpha_i(Z)n_i]N(Z) + \alpha_e(Z+1)N(Z+1)n_e.$$

For simplicity we assume that all of the MSPs have a single characteristic radius of 0.8 nm (mass of 2570 amu assuming a

Please cite this article as: Robertson, S., et al., Detection of meteoric smoke particles in the mesosphere by a rocket-borne mass spectrometer. Journal of Atmospheric and Solar-Terrestrial Physics (2013), http://dx.doi.org/10.1016/j.jastp.2013.07.007

smoke density of 2 g/cm^3) and we assume $\alpha_{ie}=10^{-6}$ cm^3 s^{-1} for consistency with previous work (Jensen and Thomas, 1991; Rapp and Lübken, 2001). The model does not account for MSP density variation with altitude; the total number density of MSPs is adjusted to a constant value of 20,000 cm^{-3}, which approximately reproduces the observed number densities of charged MSPs in the nighttime data at altitudes of 60–70 km. Solutions are obtained for a set of ionization rates Q that span the values expected from 60 to 100 km in order to represent a range of altitudes. Gumbel et al. (2003) have presented a model for the variation of Q with altitude for selected solar zenith angles. At 70 km, the ionization rate is predominantly from cosmic rays, is nearly independent of solar zenith angle, and typically $Q\cong0.04$ cm^{-3} s^{-1}. At 100 km, the ionization rate varies from a typical daytime value of $Q\cong3000$ cm^{-3} s^{-1} (from solar UV) to a nighttime typical value of $Q\cong1$ cm^{-3} s^{-1} (from geocoronal Lyman alpha radiation). In the absence of charged MSPs and negative ions, it can be assumed that $n_e=n_i$ and then $n_e=\sqrt{Q/\alpha_{ie}}$. The measured electron densities, Fig. 9, indicate that Q values are higher at a given altitude for the nighttime data except below about 75 km.

The number density of electrons, ions, and MSPs in each charge state as a function of Q are shown in Fig. 21a and b. These plots are similar to those made by Reid (1997) but the number density of MSPs has been adjusted to 20,000 cm^{-3} for consistency with the data from the CHAMPS rockets. Fig. 21c shows the modeled charged fractions versus electron density which permits a more direct comparison of model predictions with flight observations. The plot shows that as the electron density approaches zero below 70 km, the fraction of positively and negatively charged MSPs becomes nearly equal with each fraction at ~10% of the total MSP density. The positively charged fraction decreases with increasing electron density and is negligible for electron densities greater than ~100 cm^{-3}. In contrast, the negatively charged fraction increases with increasing electron density such that for electron densities > ~1000 cm^{-3} nearly 100% of the MSPs are negatively charged. A sensitivity study showed that for densities from 5000 cm^{-3} to 20,000 cm^{-3}, the charged fractions are independent of the total MSP number density. In order to better understand the altitude dependence of the charge fraction given changing electron density (ionization rate) and total MSP number density, the positive and negative charge fractions for total MSP number densities approaching zero are also shown in Fig. 21c. The limiting behaviors show that for total number density less than 5000 cm^{-3}, the majority of MSPs are negatively charged at both low and high altitudes.

The behavior at low ionization rates (low electron densities) can be explained as follows. As a consequence of a low density of ions available for recombination, an electron from ionization will either charge a neutral particle or neutralize a positive particle. An analogous situation exists for ions. For both electrons and ions, the rate coefficients for neutralizing a charged MSP are about 8 times the rate coefficient for charging a neutral MSP. Hence the number density of charged MSPs of either sign must be about 10% of the total number density for the rates of charging and discharging to be equal. These results should be viewed with caution because Natanson's rates are based upon classical physics and MSPs are sufficiently small to require quantum mechanics for an accurate calculation of capture rates. Progress in this direction is underway as quantum mechanical calculations have recently been used to find the ionization potentials of some candidate MSP materials (Rapp et al., 2012).

The model predictions are consistent with the daytime and nighttime data which show the positively charged MSPs only existing below ~70 km and the negative charged MSPs persisting throughout the full range of MSP occurrence altitudes. Furthermore, the nighttime data show these two charge populations occur in near equal abundance at altitudes below 70 km.

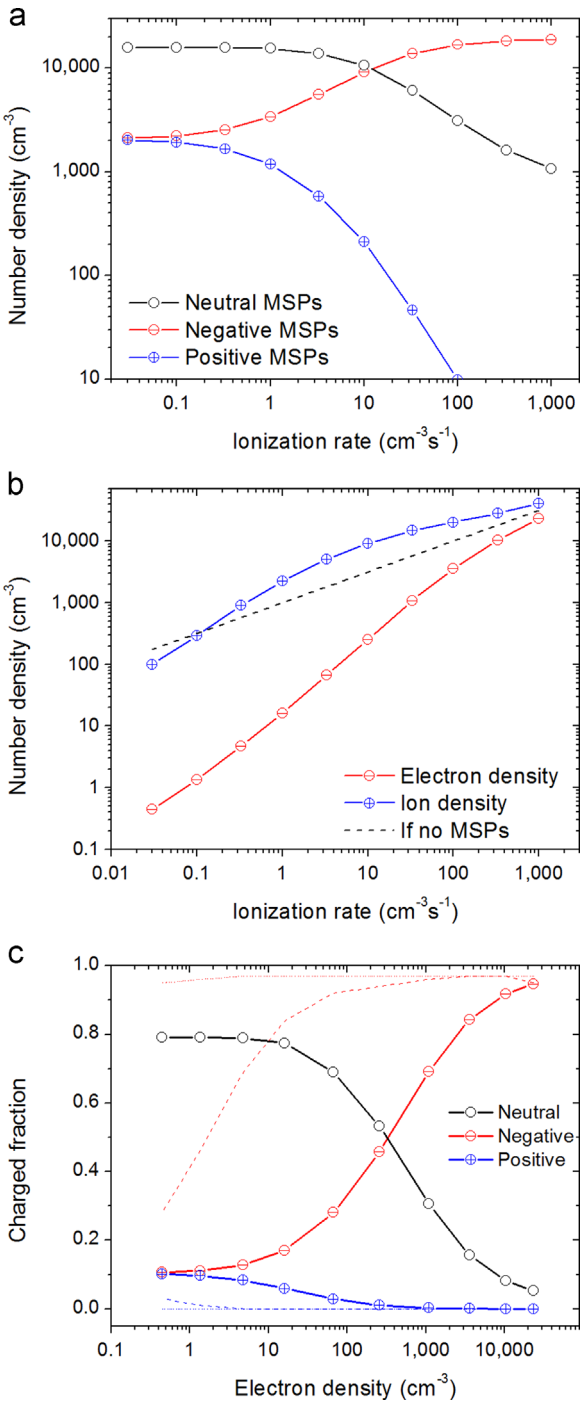

Fig. 21. Charging model predictions for (a) the number densities of charged and neutral MSPs and (b) the number densities of electrons and ions as a function of the ionization rate. The assumed total number density of MSPs is 20,000 cm^{-3}. The dashed line of (b) is the number density of electrons or ions if electron–ion recombination is their only loss mechanism. (c) Charging model predictions (applicable for total MSP number densities of 5000–20,000 cm^{-3}) presented as the charged fraction of MSPs versus free electron density. The limiting behavior of the positive and negative charge fractions as the total MSP number density is reduced are given by the dashed lines (MSP density of 2000 cm^{-3}) and dotted lines (MSP density of 100 cm^{-3}).

The model does not reproduce the near absence of negatively charged MSPs at 60–75 km in the daytime data. Rapp (2009) showed that MSPs of hematite would not be negatively charged in the daytime due to photodetachment for ambient electron number densities below ~1000 cm^{-3}. The data also indicate an abrupt reduction in negative charge density above 80 km that is not

Please cite this article as: Robertson, S., et al., Detection of meteoric smoke particles in the mesosphere by a rocket-borne mass spectrometer. Journal of Atmospheric and Solar-Terrestrial Physics (2013), http://dx.doi.org/10.1016/j.jastp.2013.07.007

indicated by the model. Possible improvements to the model that might explain these phenomena would be the addition of

- a distribution in sizes of MSPs with few above about 1 nm in radius,
- a number density and size distribution varying with altitude as seen in models with coagulation and sedimentation,
- rate coefficients for electron and ion attachment based upon quantum mechanical modeling,
- creation and destruction of negative ions,
- photodetachment of electrons from MSPs,
- the role of atomic oxygen (from photolysis of O_2) which is more abundant in the daytime (Plane, 2003). The electron affinity of atomic oxygen (1.45 eV) is probably too low for it to take electrons from MSPs directly, but it acts indirectly on charge balance through destruction of negative ions.

4.2. CARMA/CHEM2D model

In order to compare the data more directly with a model for MSP number densities, the two-dimensional CARMA/CHEM2D model (Megner et al., 2008a) was run to obtain the seasonal variation of the MSP concentration for latitude of 68°N, corresponding approximately to the launch location. This model is a coupling between the chemical dynamical CHEM2D model (Siskind et al., 1997, 2003; Summers et al., 1997), which is used to transport and sediment the meteoric material, and the microphysical CARMA model (Turco et al., 1979, Toon et al., 1979), which is used to treat particle coagulation. The model assumes a meteoric input of 44 t/day (Hughes, 1978), a meteoric ablation profile maximizing close to 85 km (Kalashnikova et al., 2000), and a smoke density of 2 g/cm^3 (Rosinski and Snow, 1961). As stated in Section 1, these quantities are not well known and they affect the modeling outcome (Megner et al., 2006). The model has 28 MSP size bins, ranging from 0.2 nm, representing the molecular size that is thought to be the end product of the ablation, to 80 nm. Modeling shows that the total number density of modeled MSPs is very sensitive to the choice of minimum radius because the initial number of smallest particles is adjusted to keep the influx of material constant; however, the number of particles above ~0.45 nm (~500 amu) is insensitive to this minimum radius. The model domain reaches from sea level to approximately 114 km, with a resolution of 4.9° in latitude and 2.6 km in altitude. The continuous influx of freshly ablated material is evenly distributed throughout the globe with an altitude distribution according to the ablation profile. The particles then coagulate and sediment while being transported by the atmospheric circulation. The seasonal variation of number densities for 68°N is shown in Fig. 22. The plot is for particles with radii greater than 0.5 nm. The model shows that the October launches occurred with number densities typical of winter conditions.

The model output for the MSP density as a function of altitude for 68°N and 8 October is shown in Fig. 23. The particles in the model have been grouped into bins corresponding approximately to the mass ranges collected on the electrodes of the MASS instrument. The model number density for particles with masses 460–1900 amu (radii 0.45–0.72 nm) reaches a maximum of ~5000 cm^{-3} at about 83 km. The measured number for the nighttime launch in the corresponding mass range (electrode 2) was ~2000 cm^{-3} for each sign of charge and the total number is estimated to be 10 times this value or ~20,000 cm^{-3}. Thus the number density in the model is about a factor of four less than the estimate based on the data and the modeled charged fraction. The model number density in the 0–460 amu (0–0.45 nm) range reaches ~70,000 cm^{-3}, with high sensitivity to the smallest

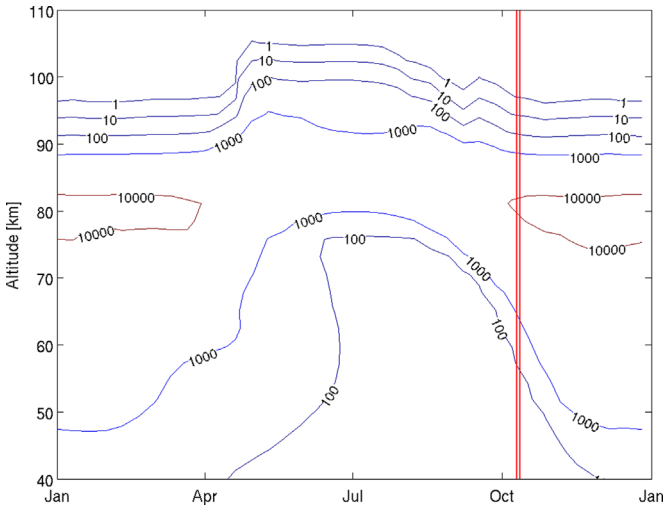

Fig. 22. Seasonal variation of MSP number densities from the CARMA/CHEM2D model for latitude 68°N. The contours indicate the number density of particles with radii exceeding 0.5 nm. The launch times are indicated by vertical lines.

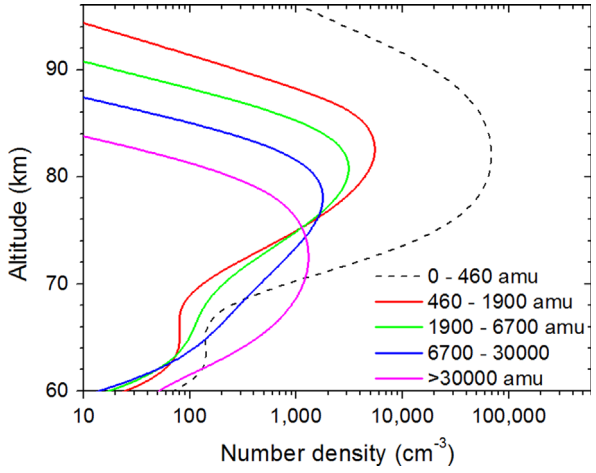

Fig. 23. MSP number densities from the CARMA/CHEM2D model for the approximate time and location of the launches. The particle radii have been converted to mass using an assumed density of 2 g/cm^3. The minimum particle radius in the model is 0.2 nm corresponding to about 40 amu.

assumed radius. The data for the corresponding mass range for the night launch show 4000 cm^{-3} of negatively charge MSPs and ions and this number would indicate 40,000 cm^{-3} if the same scale factor of 10 is applied.

5. Discussion

5.1. Total number density of MSPs

At 60–70 km altitude, the nighttime data show that the 500–2000 amu mass range has a maximum in the number density of 2000 cm^{-3} for both positively and negatively charged MSPs. The charge model indicates that the total number of MSPs is about 10 times the number density in either sign of charge; hence the data together with the charge model indicate a total number density of about 20,000 cm^{-3} in this range of masses and at 60–70 km altitude. Inclusion of the 0–500 amu mass range could double this value if the majority of these particles are MSPs rather than "ordinary" molecular ions. The total number density is additionally uncertain because the ratio of charged MSPs to uncharged

Please cite this article as: Robertson, S., et al., Detection of meteoric smoke particles in the mesosphere by a rocket-borne mass spectrometer. Journal of Atmospheric and Solar-Terrestrial Physics (2013), http://dx.doi.org/10.1016/j.jastp.2013.07.007

depends on the cross sections for collecting charge which can only be estimated because the particles are sufficiently small to require quantum mechanics for an accurate description of the attachment cross sections rather than the classical mechanics in Natanson's model.

5.2. Altitude range of MSPs

The nighttime data show the number densities of negatively charged MSPs in the 500–2000 amu mass range falling to below 30 cm^{-3} above 94 km. This highest altitude for MSP observation does not result from a falling charged fraction because the electron number density is constant or increasing from 90 to 115 km. Therefore, the rapid decrease in abundance of negatively charged MSPs above 94 km indicates a small abundance of MSPs, independent of charge. The daytime data are less clear because of spurious signals from photoemission, but there is no reason to expect the limiting altitude to vary between day and night. This upper boundary from the nighttime data agrees well the with CARMA/CHEM2D model. The lower bound from this model is at 55 km which is unfortunately below the range of the acquired data. The model also shows a maximum in the number density at about 84 km. This maximum is difficult to find in the data because the charged fraction is rapidly changing at this altitude.

5.3. Mass range and size of MSPs

The data for both launches show charged MSPs for masses up to 8000 amu, while the signals for both positive and negative MSPs in the higher mass range 8000–20,000 amu is negligible (below 10 cm^{-3}), except where the signal is likely from spurious charge. For an assumed mass density of 2 g/cm^3, the radius corresponding to 8000 amu is 1.2 nm. There is no reason for the charged fraction to be significantly different for radii greater than 1.2 nm, thus the data indicate that few of the particles have a radius greater than this value. The range of sizes detected by the MASS instrument is consistent with the characteristic sizes from radar data of 0.8 nm deduced by Strelnikova et al. (2007) and of 0.5–1.6 nm deduced by Fentzke et al. (2009, 2012). (Their results for the altitude profile of the MSP number density, which are very model dependent, differ from the values presented here.) The CARMA/CHEM2D model finds that only 4% of the particles have radii greater than 1 nm, but these have most of the mass from meteor ablation. The relationship between mass and size will be quite different if MSPs are the fluffy aggregates that have been seen in some experiments to determine the chemical end state of ablated meteoric metals (Saunders and Plane, 2006).

5.4. Charged fraction of MSPs

The charge model indicates that for both daytime and nighttime conditions, nearly 100% of MSPs are negatively charged at altitudes greater than ~80 km. This boundary is approximately the altitude at which the electron number density exceeds the MSP density. The data and charge model agree that positively charged MSPs only occur below about 75 km (where electron densities drop below 1000 cm^{-3}) for both day and nighttime conditions, with a maximum charge fraction of ~10% of the total MSP density. At these lower altitudes at night, negatively charged MSPs occur in approximately the same abundance as positively charged MSPs. During the day, the negatively charged MSP number densities are significantly reduced, likely due to photodetachment. The rocket did not return data below 60 km, however, the CARMA/CHEM2D model show that the number density of MSPs is reduced and the charging model for lower MSP densities shows that the negatively charged fraction persists to lower altitudes than the positively charged fraction.

5.5. Implications for instrumentation and modeling

The simultaneous occurrence of approximately equal numbers of positively and negatively charged MSPs below about 75 km at night indicates that instruments that record net charge, such as Faraday cups and impact detectors, are likely to find charge densities too low as a consequence of charge cancellation, in addition to the signals being reduced by aerodynamic effects. The charge on MSPs being largely negative above 80 km and approximately equally negative and positive below 75 km suggests that models for coagulation should be modified to include the effects of particle charge. The charging model of Section 4.1 indicates that the charge densities of the various species vary smoothly with ionization rate (and hence altitude), but the data have ledges in the number density of both electrons and charged MSPs that are much more abrupt than indicated by the model. The charge model also does not reproduce the near absence of negatively charged MSPs at low altitudes observed during the day. These discrepancies indicate a need for further development of models with a more complete set of rate equations that includes photodetachment, negative ions, and other charged species.

Acknowledgments

The authors thank Michael Gausa, Scott Knappmiller, Rick Kohnert, Devin Konecny, Tyler Nickerson, and the staff of the Wallops Flight Facility. This research was support by the NASA Low Cost Access to Space program.

References

Amyx, K., Sternovsky, Z., Knappmiller, S., Robertson, S., Horányi, M., Gumbel, J., 2008. In-situ measurement of smoke particles in the winter polar mesosphere between 80 and 85 km altitude. Journal of Atmospheric and Solar-Terrestrial Physics 70, 61070.

Bardeen, C.G., Toon, O.B., Jensen, E.J., Marsh, D.R., Harvey, V.L., 2008. Numerical simulations of the three-dimensional distribution of meteoric dust in the mesosphere and upper stratosphere. Journal of Geophysics Research 113, D17202, http://dx.doi.org/10.1029/2007JD009515.

Bennett, F.D.G., Hall, J.E., Dickinson, P.H.G., 1972. D-Region electron densities and collision frequencies from Faraday rotation and differential absorption. Journal of Atmospheric and Terrestrial Physics 34, 1321–1335.

Bird, G.A., 1988. Aerodynamic effects on atmospheric composition measurements from rocket vehicles in the thermosphere. Planetary and Space Science 36, 921–926.

Bird, G.A., 1994. Molecular Gas Dynamics and the Direct Simulation of Gas Flows. Oxford University Press, New York.

Bremer, J., Hoffmann, P., Latteck, R., Singer, W., 2003. Seasonal and long-term variations of PMSE from VHF radar observations at Andenes, Norway. Journal of Geophysics Research 108 (8), 8438.

Curtius, J., Weigel, R., Vössing, H.-J., Wernli, H., Werner, A., Volk, C.-M., Konopka, P., Krebsbach, M., Schiller, C., Roiger, A., Schlager, H., Dreiling, V., Borrmann, S., 2005. Observations of meteoric material and implications for aerosol nucleation in the winter Arctic lower stratosphere derived from in situ particle measurements. Atmospheric Chemistry and Physics 5, 3053–3069.

Dalmann, B.K., Grün, E., Kissel, J., Dietzel, H., 1977. The ion-composition of the plasma produced by impacts of fast dust particles. Planetary and Space Science 25, 135–147.

Dickson, S., Gausa, M., Robertson, S., Sternovsky, Z., 2013. Channel electron multiplier operated on a sounding rocket from 120 to 80 km altitude. Journal of Atmospheric and Solar-Terrestrial Physics 95–96, 51–58.

Fentzke, J.T., Janches, D., Strelnikova, I., Rapp, M., 2009. Meteoric smoke particle properties derived using dual-beam Arecibo UHF observations of D-region spectra during different seasons. Journal of Atmospheric and Solar-Terrestrial Physics 71, 1982–1991.

Fentzke, J.T., Hsu, V., Brum, C.G.M., Strelnikova, I., Rapp, M., Nicolls, M., 2012. D region meteoric smoke and neutral temperature retrieval using the poker flat incoherent scatter radar. Geophysics Research Letters 39, L21101.

Folkestad, K., 1970. Ionospheric studies by in situ measurements in sounding rockets. Internal NDRE Report 59 (and Ph.D. Thesis University of Oslo).

Please cite this article as: Robertson, S., et al., Detection of meteoric smoke particles in the mesosphere by a rocket-borne mass spectrometer. Journal of Atmospheric and Solar-Terrestrial Physics (2013), http://dx.doi.org/10.1016/j.jastp.2013.07.007

Friedrich, M., Finsterbusch, R., Torkar, K.M., Spöcker, P., 1991. A further generalisation of the Sen and Wyller magneto-ionic theory. Advance earch 11, 105–108.
Friedrich, M., Rapp, M., Blix, T., Hoppe, U.-P., Torkar, K.M., Robertson, S., Dickson, S., Lynch, K., 2012. Electron loss and meteoric dust in the mesosphere. Annales de Geophysique 30, 1495–1501.
Gabrielli, P., Barbante, C., Plane, J.M.C., Varga, A., Hong, S., Cozzi, G., Gasparia, V., Planchon, F.A.M., Cairns, W., Ferrari, C., Crutzen, P., Ceson, P., Boutron, C.F., 2004. Meteoritic smoke fallout over the Holocene epoch revealed by iridium and platinum in Greenland ice. Nature 432, 1011–1014.
Gelinas, L.J., Lynch, K.A., Kelley, M.C., Collins, S., Baker, S., Zhou, Q., Friedman, J.S., 1998. First observation of meteoric charged dust in the tropical mesosphere. Geophysics Research Letters 25, 4047–4050.
Gelinas, L.J., Lynch, K.A., Kelley, M.C., Collins, R.L., Widholm, M., MacDonald, E., Ulwick, J., Mace, P., 2005. Mesospheric charged dust layer: implications for neutral chemistry. Journal of Geophysics Research 110, A01310.
Gumbel, J., Megner, L., 2009. Charged meteoric smoke as ice nuclei in the mesosphere: Part 1 – A review of basic concepts. Journal of Atmospheric and Solar-Terrestrial Physics 71, 1225–1235.
Gumbel, J., Siskind, D.E., Witt, G., Torkar, K.M., Friedrich, M., 2003. Influences of ice particles on the polar summer mesosphere. Journal of Geophysics Research 108 (D8), 8436.
Havnes, O., Næsheim, L.I., 2007. On the secondary charging effects and structure of mesospheric dust particles impacting on rocket probes. Annales de Geophysique 25, 623–637.
Havnes, O., Trøim, J., Blix, T., Mortensen, W., Næsheim, L.I., Thrane, E., Tønnesen, T., 1996. First detection of charged dust particles in the Earth's mesosphere. Journal of Geophysics Research 101, 10839–10847.
Havnes, O., Kassa, M., 2009. On the sizes and observable effects of dust particles in polar mesospheric winter echoes. Journal of Geophysics Research 114, D09209.
Havnes, O., de Angelis, U., Bingham, R., Goertz, C.K., Morfill, G.E., Tsytovich, V., 1990. On the role of dust in the summer mesopause. Journal of Atmospheric and Terrestrial Physics 52, 637–643.
Havnes, O., La Hoz, C., Rietveld, M.T., Kassa, M., Baroni, G., Biebricher, A., 2011. Dust charging and density conditions deduced from observations of PMWE modulated by artificial electron heating. Journal of Geophysical Research 116 (D24), D24203.
Hedin, J., Gumbel, J., Rapp, M., 2007. On the efficiency of rocket-borne particle detection in the mesosphere. Atmospheric Chemistry and Physics 7, 3701–3711.
Hershkowitz, N., Auciello, O., Flamm, D. (Eds.), 1989. Plasma Diagnostics. Academic, San Diego. (p. 113).
Hervig, M.E., Gordley, L.L., Deaver, L.E., Siskind, D.E., Stevens, M.H., Russell, J.M., Bailey, S.M., Megner, L., Bardeen, C.G., 2009. First satellite observations of meteoric smoke in the middle atmosphere. Geophysics Research Letters 36, L18805.
Hervig, M.E., Deaver, L.E., Bardeen, C.G., Russell, J.M., Bailey, S.M., Gordley, L.L., 2012. The content and composition of meteoric smoke in the mesospheric ice particle from SOFIE observations. Journal of Atmospheric and Solar-Terrestrial Physics 84–85, 1–6.
Horányi, M., Gumbel, J., Witt, G., Robertson, S., 1999. Simulation of rocket-borne particle measurements in the mesosphere. Geophysics Research Letters 26, 1537–1540.
Hughes, D.W., 1978. Cosmic Dust. John Wiley & Sons, Chichester.
Hunten, D.M., Turco, R.P., Toon, O.B., 1980. Smoke and dust particles of meteoric origin in the mesosphere and stratosphere. Journal of the Atmospheric Sciences 37, 1342–1357.
Jacobsen, T.A., Friedrich, M., 1979. Electron density measurements in the lower D-region. Journal of Atmospheric and Terrestrial Physics, 41; , pp. 1195–1200.
Janches, D., Dryud, L.P., Broadley, S.L., Plane, J.M.C., 2009. First observation of micrometeoroid ablation in the atmosphere. Geophysics Research Letters 36, L06101.
Jensen, E., Thomas, G.E., 1991. Charging of mesospheric particles: implications of electron density and particle coagulation. Journal of Geophysics Research 96, 18,603–18,615.
Kalashnikova, O., Horányi, M., Thomas, G.E., Toon, O.B., 2000. Meteoric smoke production in the atmosphere. Geophysics Research Letters 27 (329), 3–3296.
Kassa, M., Rapp, M., Hartquist, T.W., Havnes, O., 2012. Secondary charging effects due to icy dust particle impacts on rocket payloads. Annales de Geophysique 30, 433–439.
Kavanagh, A.J., Honary, F., Rietveld, M.T., Senior, A., 2006. First observations of the artificial modulation of polar mesospheric winter echoes. Geophysics Research Letters 33, L19801.
Klumov, B.S.A., Popel, S.I., Bingham, R., 2000. Dust particle charging and formation of dust structures in the upper atmosphere. JETP Letters 72, 524–529.
Klumov, B.A., Morfill, G.E., Popel, S.I., 2005. Formation of structures in a dusty ionosphere. Journal of Experimental and Theoretical Physics 100, 152–164. (English Translation).
Knappmiller, S., Robertson, S., Sternovsky, Z., Friedrich, M., 2008. A rocket-borne mass analyzer for charged aerosol particles in the mesosphere. Review of Scientific Instruments 79, 104502.
Knappmiller, S., Rapp, M., Robertson, S., Gumbel, J., 2011. Charging of meteoric smoke and ice particles in the mesosphere including photoemission and photodetachment rates. Journal of Atmospheric and Solar-Terrestrial Physics 73, 2212–2220.
La Hoz, C., Havnes, O., 2008. Artificial modification of polar mesospheric winter echoes with an RF heater: do charged dust particles play an active role? Journal of Geophysics Research 113, D19205.
Lübken, F.-J., Fricke, K.-H., Langer, M., 1996. Noctilucent clouds and the thermal structure near the Arctic mesopause in summer. Journal of Geophysics Research 101, 9489–9508.
Lynch, K.A., Gelinas, L.J., Kelley, M.C., Collins, R.L., Widholm, M., Rau, D., MacDonald, E., Liu, Y., Ulwick, J., Mace, P., 2005. Multiple sounding rocket observations of charged dust in the polar winter mesosphere. Journal of Geophysics Research 110, A03302, http://dx.doi.org/10.1029/2004JA010502.
Mechtly, E.A., Bowhill, S.A., Smith, L.G., Knoebel, H.W., 1967. Lower ionosphere electron concentrations and collision frequency from rocket easurements of Faraday rotation, differential absorption, and probe current. Journal of Geophysics Research 72, 5239–5245.
Megner, L., Gumbel, J., 2009. Charged meteoric particles as ice nuclei in the mesosphere: Part 2 – A feasibility study. Journal of Atmospheric and Solar-Terrestrial Physics 71, 1237–1244.
Megner, L., Rapp, M., Gumbel, J., 2006. Distribution of meteoritic smoke – sensitivity to microphysical properties and atmospheric conditions. Atmospheric Chemistry and Physics 6, 4415–4426.
Megner, L., Siskind, D.E., Rapp, M., Gumbel, J., 2008a. Global and temporal distribution of meteoric smoke: a two-dimensional study. Journal of Geophysics Research 113, D03202.
Megner, L., Gumbel, J., Rapp, M., Siskind, D.E., 2008b. Reduced meteoric smoke particle density at the summer pole – implications for mesospheric ice particle nucleation. Advance Space Research 41, 41–49.
Natanson, G.L., 1960. On the theory of the charging of microscopic aerosol particles as a result of capture of gas ions. Soviet Physics Technical Physics (English translation) 5, 538–551.
Plane, J.M.C., 2003. Atmospheric chemistry of meteoritic metals. Chemical Reviews 103, 4963–4984.
Plane, J.M.C., 2011. On the role of metal silicate molecules as ice nuclei. Journal of Atmospheric and Solar-Terrestrial Physics 73. (2192–2100).
Plane, J.M.C., 2012. Cosmic dust in the earth's atmosphere. Chemical Society Reviews 41, 6507–6518.
Rapp, M., 2009. Charging of mesospheric aerosol particles: the role of photodetachment and photoionization from meteoric smoke and ice particles. Annales de Geophysique 27, 2417–2422.
Rapp, M., Lübken, F.-J., 2004. Polar mesosphere summer echoes (PMSE): review of observations and current understanding. Atmospheric Chemistry and Physics 4, 2601–2633.
Rapp, M., Lübken, F.-J., 2001. Modelling of particle charging in the polar summer mesosphere: Part 1 – General results. Journal of Atmospheric and Solar-Terrestrial Physics 63, 759–770.
Rapp, M., Strelnikova, I., 2009. Measurements of meteor smoke particles during the ECOMA-2006 campaign: 1. Particle detection by active photoionization. Journal of Atmospheric and Solar-Terrestrial Physics 71, 477–485.
Rapp, M., Strelnikov, B., Wilms, S., Lübken, F.-J., Gumbel, J., Henkel, H., 2003. A new detector for the in situ measurement of meteoric dust particles in the middle atmosphere. In: Proceedings of the 16th ESA symposium on European Rocket and Balloon Programmes. St. Gallen, Switzerland (ESA SP-530).
Rapp, M., Strelnikova, I., Gumbel, J., 2007. Meteoric smoke particles: evidence from rocket and radar techniques. Advance Space Research 40, 809–817.
Rapp, M., Strelnikova, I., Strelnikov, B., Hoffmann, P., Friedrich, M., Gumbel, J., Megner, L., Hoppe, U.-P., Robertson, S., Knappmiller, S., Wolff, M., Marsh, D., 2009. Rocket-borne in-situ measurements of meteor smoke: charging properties and implications for seasonal variation. Journal of Geophysics Research 115, D00I16.
Rapp, M., Strelnikova, I., Strelnikov, B., Hoffmann, P., Friedrich, M., Gumbel, J., Megner, L., Hoppe, U.-P., Robertson, S., Knappmiller, S., Wolff, M., Marsh, D., 2010. Rocket-borne in-situ measurements of meteor smoke: charging properties and implications for seasonal variation. Journal of Geophysics Research 115, D00I16.
Rapp, M., Plane, J.M.C., Strelnikov, B., Stober, G., Ernst, S., Hedin, J., Friedrich, M., Hoppe, U.-P., 2012. In situ observation of meteor smoke particles (MSP) during the Geminids 2012: constraints on MSP size, work function and composition. Annales de Geophysique 30, 1661–1673.
Reid, G.C., 1990. Ice particles and electron "bite-outs" at the summer polar mesopause. Journal of Geophysics Research 95, 13,891–13,896.
Reid, G.C., 1997. On the influence of electrostatic charging on coagulation of dust and ice particles in the upper mesosphere. Geophysics Research Letters 24, 1095–1098.
Robertson, S., Smiley, B., Horányi, M., Sternovsky, Z., Gumbel, J., Stegman, J., 2004. Rocket-borne probes for charged ionospheric aerosol particles. IEEE Transactions on Plasma Science 32, 716–723.
Robertson, S., Horányi, M., Knappmiller, S., Sternovsky, Z., Holzworth, R., Shimogawa, M., Friedrich, M., Torkar, K., Gumbel, J., Megner, L., Baumgarten, G., Latteck, R., Rapp, M., Hoppe, U.-P., Hervig, M.E., 2009. Mass analysis of charged aerosol particles in NLC and PMSE during the ECOMA/MASS campaign. Annales de Geophysique 27, 1213–1232.
Rosinski, J., Snow, R.H., 1961. Secondary particulate matter from meteor vapors. Journal of Meteorology 18, 736–745.
Saunders, R.W., Plane, J.M.C., 2006. A laboratory study of meteor smoke analogues: composition, optical properties, and growth kinetics. Journal of Atmospheric and Solar-Terrestrial Physics 68, 2182–2202.

Please cite this article as: Robertson, S., et al., Detection of meteoric smoke particles in the mesosphere by a rocket-borne mass spectrometer. Journal of Atmospheric and Solar-Terrestrial Physics (2013), http://dx.doi.org/10.1016/j.jastp.2013.07.007

Sen, H.K., Wyller, A.A., 1960. On the generalization of the Appleton–Hartree magnetoionic formulas. Journal of Geophysics Research 65, 3931–3950.

Siskind, D.E., Bacmeister, J.T., Summers, M.E., Russell, J.M., 1997. Two-dimensional model calculations of nitric oxide transport in the middle atmosphere and comparison with Halogen Occultation Experiment data. Journal of Geophysics Research 102, 3527–3545.

Siskind, D.E., Eckermann, S.D., McCormack, J.P., Alexander, M.J., Bacmeister, J.T., 2003. Hemispheric differences in the temperature of the summertime stratosphere and mesosphere. Journal of Geophysics Research 108 (D2), 4051, http://dx.doi.org/10.1029/2002JD002095.

Smiley, B., Robertson, S., Horányi, M., Blix, T., Rapp, M., Latteck, R., Gumbel, J., 2003. Measurement of positively and negatively charged particles inside PMSE during MIDAS SOLSTICE 2001. Journal of Geophysics Research 108 (D8), 8444. (10 pp.).

Strelnikova, I., Rapp, M., Raizada, S., Sulzer, M., 2007. Meteor smoke particle properties derived from Arecibo incoherent scatter radar observations. Geophysics Research Letters 34, L15815.

Strelnikova, I., Rapp, M., Streknikov, B., Baumgarten, G., Brattli, A., Svenes, K., Hoppe, U.-P., Friedrich, M., Gumbel, J., Williams, B.P., 2009. Measurements of meteor smoke particles during the ECOMA-2006 campaign: 2. Results. Journal of Atmospheric and Solar-Terrestrial Physics 71, 486–496.

Summers, M.E., Siskind, D.E., Bacmeister, J.T., Conway, R.R., Zasadil, S.E., Strobel, D.F., 1997. Seasonal variation of middle atmospheric CH_4 and H_2O with a new chemical dynamical model. Journal of Geophysics Research 102, 3503–3526.

Thomas, L., Bowman, M.R., 1985. Model studies of the D-region negative-ion concentration during day-time and night-time. Journal of Atmospheric and Terrestrial Physics 47, 547.

Toon, O.B., Turco, R.P., Hamill, P., Kiang, C.S., Whitten, R.C., 1979. A one-dimensional model describing aerosol formation and evolution in the stratosphere: II. Sensitivity studies and comparison with observations. Journal of the Atmospheric Sciences 36, 718–736.

Turco, R.P., Hamill, P., Toon, O.B., Whitten, R.C., Kiang, C.S., 1979. A one-dimensional model describing aerosol formation and evolution in the stratosphere: I. Physical processes and mathematical analogs. Journal of the Atmospheric Sciences 36, 699–717.

Vondrak, T., Plane, J.M.C., Broadley, S., Janches, D., 2008. A chemical model of meteoric ablation. Atmospheric Chemistry and Physics 8, 7015–7031.

Williams, B.P., Fritts, D.C., She, C.Y., Goldberg, R.A., 2006a. Gravity wave propagation through a large semidiurnal tide and instabilities in the mesosphere and lower thermosphere during the winter 2003 MaCWAVE rocket campaign. Annales de Geophysique 24, 1199–1208. (Sref-ID: 1432-0576/ag/2006-24-1199).

Williams, B.P., Vance, J.D., She, C.-Y., Fritts, D.C., Abe, T., Thrane, E., 2006b. Sodium lidar measurements of waves and instabilities near the mesopause during the DELTA rocket campaign. Earth, Planets, and Space 58, 1131–1137.

Witt, G., 1969. The nature of noctilucent clouds. Space Research 9, 157–169.

Please cite this article as: Robertson, S., et al., Detection of meteoric smoke particles in the mesosphere by a rocket-borne mass spectrometer. Journal of Atmospheric and Solar-Terrestrial Physics (2013), http://dx.doi.org/10.1016/j.jastp.2013.07.007